

GALAXIA: A CODE TO GENERATE A SYNTHETIC SURVEY OF THE MILKY WAY

SANJIB SHARMA, JOSS BLAND-HAWTHORN¹

Sydney Institute for Astronomy, School of Physics, University of Sydney, NSW 2006, Australia

KATHRYN V JOHNSTON

Department of Astronomy, Columbia University, New York, NY-10027

JAMES BINNEY

Rudolf Peierls Centre for Theoretical Physics, 1 Keble Rd, Oxford, OX1 3NP, UK

Draft version May 28, 2018

ABSTRACT

We present here a fast code for creating a synthetic survey of the Milky Way. Given one or more color-magnitude bounds, a survey size and geometry, the code returns a catalog of stars in accordance with a given model of the Milky Way. The model can be specified by a set of density distributions or as an N-body realization. We provide fast and efficient algorithms for sampling both types of models. As compared to earlier sampling schemes which generate stars at specified locations along a line of sight, our scheme can generate a continuous and smooth distribution of stars over any given volume. The code is quite general and flexible and can accept input in the form of a star formation rate, age metallicity relation, age velocity dispersion relation and analytic density distribution functions. Theoretical isochrones are then used to generate a catalog of stars and support is available for a wide range of photometric bands. As a concrete example we implement the Besançon Milky Way model for the disc. For the stellar halo we employ the simulated stellar halo N-body models of Bullock & Johnston (2005). In order to sample N-body models, we present a scheme that disperses the stars spawned by an N-body particle, in such a way that the phase space density of the spawned stars is consistent with that of the N-body particles. The code is ideally suited to generating synthetic data sets that mimic near future wide area surveys such as GAIA, LSST and HERMES. As an application we study the prospect of identifying structures in the stellar halo with a simulated GAIA survey. We plan to make the code publicly available at <http://galaxia.sourceforge.net>.

Subject headings: Galaxy: stellar content – structure – methods: data analysis – numerical

1. INTRODUCTION

Generating a synthetic catalog of stars in accordance with a given model of galaxy formation has a number of uses. First, it helps to interpret the observational data. Secondly, it can be used to test the theories upon which the models are based. Moreover synthetic catalogs can be used to test the capabilities of different instruments, check for systematics and device strategies to reduce measurement errors. This is well understood by the architects of galaxy redshift surveys who rely heavily on Λ CDM simulations to remove artifacts imposed by the observing strategy (Colless et al. 2001).

Given the widespread use of synthetic catalogs, a need for faster and accurate methods to generate stellar synthetic catalogs has recently arisen due to the advent of large scale surveys in astronomy, e.g., future surveys like LSST and GAIA have plans to measure over 1 billion stars. In order to generate a synthetic catalog, one first needs to have a model of the Milky Way. While we are far from a dynamically consistent model, a working framework is fundamental to progress. Inevitably, this will require approximations or assumptions that may not be mutually consistent. Cosmologists already accept such compromises when they relate the observed galaxies to the dark-matter test particles that emerge from cosmological simulations.

There have been various attempts over the past few decades

to create a Galaxy model that is constrained by observations. The earliest such attempt was by Bahcall & Soneira (1980a,b, 1984) where they assumed an exponential disc with magnitude dependent scale heights. An evolutionary model using population synthesis techniques was presented by Robin & Creze (1986). Given a star formation rate (SFR) and an initial mass function (IMF), one calculates the resulting stellar populations using theoretical evolutionary tracks. Local observations were then used to constrain the SFR and IMF. Bienayme et al. (1987) later introduced dynamical self consistency to constrain the disc scale height. The present state of the art is described in Robin et al. (2003) and is known as the Besançon model. Here the disc is constructed from a set of isothermal populations that are assumed to be in equilibrium. Analytic functions for density distributions, the age/metallicity relation and the IMF are provided for each population. A similar scheme is also used by the photometric code TRILEGAL (Girardi et al. 2005).

In spite of its popularity, the current Besançon model has important shortcomings. A web interface exists to generate synthetic catalogs from the model but it has limited applicability for generating wide area surveys. Discrete step sizes for radial, and angular coordinates need to be specified by the user and results might differ depending upon the chosen step size. The scale height and the velocity dispersion of the disc are in reality a function of age but, due to computational complexity, the disc is modeled as a finite set of isothermal discs of different ages. Increasing the number of discs enhances

¹ Leverhulme Visiting Professor, and Merton College Fellow, University of Oxford, OX1 3RH, UK.

the smoothness of the model but at the price of computational cost (Girardi et al. 2005).

In addition to the disc components, one also needs a model of the stellar halo. Under the hierarchical structure formation paradigm, a significant fraction of the stellar halo is thought to have been produced by accretion events and signatures of these should be visible as substructures in the stellar halo. Missions like GAIA, LSST and PanSTARRS are being planned that will enable us to detect substructures in the stellar halo.

A smooth analytic stellar halo as in the Besançon model is inadequate for testing schemes of substructure detection. Furthermore, such a halo does not accommodate known structures like the Sagittarius dwarf stream which may constitute a large fraction of the present halo (Ibata et al. 1995; Chou et al. 2010). Substructures have complex shapes and hence to model them we cannot use the approach of analytic density distributions as discussed earlier. However, N-body models are ideally suited for this task. Brown et al. (2005) attempted to combine a smooth galaxy model with some simulated N-body models of disrupting satellites, but the stellar halo was not simulated in a proper cosmological context. Using hybrid N-body techniques, Bullock & Johnston (2005) have produced high resolution N body models of the stellar halo that are simulated within a cosmological context; see also Cooper et al. (2010b) and De Lucia & Helmi (2008) for a similar approach. These can be used to make accurate predictions of the substructures in the stellar halo and also test the Λ CDM paradigm. However, as highlighted by Brown et al. (2005) there are several unresolved issues related to sampling of an N-body model and this has prevented their widespread use.

The aim of this paper is to present fast and accurate methods to convert analytic and N-body models of a galaxy into a synthetic catalog of stars. This would relieve the burden of generating catalogs from modelers on one hand and on the other hand would allow the testing of models generated by different groups. This should also facilitate rapid testing of new models.

We present a new scheme for sampling the analytical models that enables us to generate continuous values of the variables like position and age of stars. Instead of a set of discs at specified ages, our methodology allows us to generate a disc that is continuous in age. As a concrete example, we use the Besançon analytical model for the disc. To model the disc kinematics more accurately, we employ the Shu (1969) distribution function that describes the non-circular motion in the plane of the disc. For the stellar halo we use the simulated N-body models of Bullock & Johnston (2005) that can reproduce the substructure in the halo. We show a scheme for sampling the N-body particles such that the sampled stars preserve the underlying phase space density of N-body particles.

2. METHODS

2.1. Analytic framework for modeling the galaxy

We first describe the analytic framework that is used by us for modeling the Galaxy. The stellar content of the Galaxy is modeled as a set of distinct components, e.g., the thin disc, the thick disc, the stellar halo and the bulge. The distribution function, i.e., the number density of stars as a function of position (\mathbf{r}), velocity (\mathbf{v}), age (τ), metallicity (Z), and mass (m) of stars for each component is assumed to be specified a

priori. This can be expressed in general as

$$f_j = f_j(\mathbf{r}, \mathbf{v}, \tau, Z, m), \quad (1)$$

j being the label of the component. An accurate form of Equation (1) that describes all the properties of the Galaxy and is self consistent is still an open question. However, over the past few decades considerable progress has been made to arrive at a working model using a few simple assumptions (Robin & Creze 1986; Bienayme et al. 1987; Haywood et al. 1997a,b; Girardi et al. 2005; Robin et al. 2003). Our analytical framework is based upon these models and we describe this below.

For a given galactic component, let the stars be formed at a rate of $\Psi(\tau)$ and the mass distribution of stars $\xi(m, \tau)$ (IMF) be a parameterized function of age τ only. Also, let the present day spatial distribution of stars, $f_{\text{pos}}(\mathbf{r}, \tau)$ be a function of age only. Finally, assuming that the velocity distribution $f_{\text{vel}}(\mathbf{v}, \tau)$ and the metallicity distribution, $f_Z(Z, \mathbf{r}, \tau)$ are a function of age and position only one arrives at a model of the form (label j omitted for brevity)

$$f_j = \frac{\Psi(\tau)}{\langle m \rangle} \xi(m, \tau) f_{\text{pos}}(\mathbf{r}, \tau) f_{\text{vel}}(\mathbf{v}, \tau) f_Z(Z, \mathbf{r}, \tau) \quad (2)$$

Note, the functions on the right hand side can potentially take different forms for different galactic components, e.g., the thin disc, the thick disc and so on. The IMF here is normalized such that $\int_{m_{\text{min}}}^{m_{\text{max}}} \xi(m, \tau) dm = 1$ and $\langle m \rangle = \int_{m_{\text{min}}}^{m_{\text{max}}} m \xi(m) dm$ is the mean stellar mass. We now discuss the functional forms of the metallicity and the velocity distribution.

The distribution f_Z is modeled as a log-normal distribution,

$$f_Z = \frac{1}{\sigma_{\log Z}(\tau) \sqrt{2\pi}} e^{-(\log Z - \log \bar{Z}(\tau))^2 / (2\sigma_{\log Z}^2(\tau))}, \quad (3)$$

the mean and dispersion of which is given by an age-dependent function. The mean metallicity as function of age, $\bar{Z}(\tau)$, is popularly known as the age-metallicity relation (AMR). In general a spatial dependence might also be added to Equation (3), e.g., $d \log(\bar{Z})/dR = \text{constant}$.

The velocity distribution f_{vel} can be modeled as a triaxial Gaussian,

$$f_{\text{vel}} = \frac{1}{\sigma_R \sigma_\phi \sigma_z (2\pi)^{3/2}} \exp \left(-\frac{v_R^2}{2\sigma_R^2(\tau, R)} - \frac{v_z^2}{2\sigma_z^2(\tau, R)} \right) \times \exp \left(-\frac{(v_\phi - v_{\text{circ}}(R) - v_{\text{ad}}(\tau, R))^2}{2\sigma_\phi^2(\tau, R)} \right) \quad (4)$$

where, R, ϕ, z are the cylindrical coordinates, $v_{\text{circ}}(R)$ the circular velocity as a function of cylindrical radius R and v_{ad} the asymmetric drift, which is given by the Stromberg's relation (equation 4.228 in Binney & Tremaine 2008)

$$v_{\text{ad}}(\tau, R) = \frac{\sigma_R^2}{2v_c} \times \left(\frac{d \ln \rho}{d \ln R} + \frac{d \ln \sigma_\phi^2}{d \ln R} + 1 - \frac{\sigma_\phi^2}{\sigma_R^2} + 1 - \frac{\sigma_z^2}{\sigma_R^2} \right) \quad (5)$$

Alternatively, one can model the distribution of v_ϕ using the Shu (1969) distribution function (Schönrich & Binney 2009), this is described in Appendix A. The dispersions of the R, z and ϕ components of velocity increase as a function of age due

to secular heating in the disc and moreover there is also radial dependence, the dispersion is higher close to the center. We model these effects as in Binney (2010) using the following functional form

$$\sigma_{R,\phi,z}^{\text{thin}}(R, \tau) = \sigma_{R0,\phi0,z0} \left(\frac{\tau + \tau_{\min}}{\tau_{\max} + \tau_{\min}} \right)^{\beta} \left(\frac{\Sigma^{\text{thin}}(R)}{\Sigma_{\odot}^{\text{thin}}} \right)^q \quad (6)$$

where Σ is the surface density of the disc (age dependence from Aumer & Binney 2009).

The model as given by Equation (2) has some limitations. For example, Equation (2) by itself is not dynamically self consistent and this has to be imposed externally. For a given $v_{\text{circ}}(R)$, $\Psi(\tau)$ and $\sigma_z(\tau)$ the vertical structure of the disc in the solar neighborhood can be made dynamically self consistent by using the approach of Bienayme et al. (1987) (see also Just & Jahreiß 2010). This leads to a constraint of the form $\epsilon = \epsilon(\tau)$, ϵ being the ellipticity of a homoeoid disc (or scale height $h_z = h_z(\tau)$ for a double exponential disc).

The second limitation of Equation (2) is that it does not have an explicit dependence on the birth radii of a star. Recently semi-analytic models of the Galaxy that treat chemical evolution with radial mixing have been proposed by Schönrich & Binney (2009) where the properties of a star are linked to their birth radii. A possible way to accommodate such models is to introduce in Equation (2) an additional parameter R_i , the radius at which a star is born in cylindrical coordinates. The model distribution function is then given by

$$f = \frac{\Psi(\tau, R_i)}{\langle m \rangle} \xi(m, \tau) \times f_{\text{pos}}(\mathbf{r}, R_i, \tau) f_{\text{vel}}(\mathbf{v}, \mathbf{r}, R_i, \tau) f_Z(Z, R_i, \tau), \quad (7)$$

$f_{\text{pos}}(\mathbf{r}, R_i, \tau)$ being the present day spatial distribution of stars that were born τ years ago at radius R_i .

2.2. Sampling an analytic model: adaptive von Neumann rejection technique

Having specified the analytical framework we now discuss the scheme to sample stars from a model specified within this framework. In the present paper we restrict ourselves to models of the form of Equation (2) but the scheme we discuss is equally applicable to extensions of the form of Equation (7).

For a model given by Equation (2), if \mathbf{r} and τ are given, sampling the metallicity distribution and the velocity distribution is trivial. Similarly, sampling the mass of a star is also straightforward as it is a one-dimensional distribution. Once the age, metallicity and mass of a star are known, a synthetic library of isochrones can then be used to generate stellar parameters like color, magnitude, gravity and so on. So the key task is to sample the position and age coordinates from a specified analytical function

$$g(\mathbf{r}, \tau) = \frac{\Psi(\tau) f_{\text{pos}}(\mathbf{r}, \tau)}{\langle m \rangle}, \quad (8)$$

which is multidimensional.

A simple approach to sample points from an analytical multidimensional distribution as given by Equation (8) is to use the von Neumann rejection technique — generate a star having random coordinates \mathbf{r}, τ ; then generate a random number x between 0 and g_{\max} and finally accept the star if $x < g(\mathbf{r}, \tau)$. This naive approach is computationally very expensive. A lot of computational effort is spent to sample the low

density regions that require rejection of a lot of stars. Moreover, the computational time does not scale with output sample size, so to generate even a small specific sample of stars, e.g., stars lying within a given color magnitude limits or stars lying in some specific region of space, one has to generate all the stars in the galaxy.

We now discuss an efficient technique to sample a specified multidimensional distribution. We first divide the entire domain into bins that extend perpendicular to the time axis. Then we subdivide these bins into smaller sub-domains, called leaf nodes, with a spatial oct-tree (each sub node having 1/8th the volume of its parent node). Having subdivided the system, the von Neumann rejection technique is now applied individually to each of the nodes. This has two immediate advantages:

- Depending upon the given geometry of the survey, one can check if the boundaries of the node intersect with that of the survey and, if not, one can skip the generation of stars.
- For accepting and rejecting stars it is now possible to set the maximum density $g_{\max}(\mathbf{r}, \tau, \mathbf{l})$, \mathbf{l} being a vector representing the length of the sides of the node, adaptively for each node. Since the variation in stellar density in any node will be limited, g/g_{\max} will never be very small, with the consequence that the rejection sampling method will not be inefficient.

We still need to decide on an optimum truncation criterion to stop the splitting of nodes. An ideal truncation criterion is to have the least density variation within a node but this would result in a lot of nodes with negligible number of stars but an otherwise strong number density gradient. Instead, we adopt a criterion that strives to achieve a fixed number of stars in a node similar to the one used in adaptive mesh refinement schemes. For a total of N_{tot} stars, we set the resolution limit of a node as $N_{\text{tot}}/10^6$, a choice that effectively generates about 10^6 nodes. However, calculating the number of stars in a node involves an integral of the number density over the volume of the node, which can be computationally intensive when done for a large number of nodes. Hence, for the node splitting purpose, we compute the number of stars as

$$N'_{\text{node}} = g_{\max}(\mathbf{r}, \tau, \mathbf{l}) l_1 l_2 l_3 l_4 \quad (9)$$

where $g_{\max}(\mathbf{r}, \tau, \mathbf{l})$ is an analytic density function representing the maximum density within a node and l_1, l_2, l_3, l_4 are the length of the sides of the node. The final number of stars in a node, N_{node} , is calculated by numerically integrating the number density over the node with increasing spatial and temporal resolution till the number converges with an uncertainty less than $0.1\sqrt{N_{\text{node}}}$. The above convergence criterion roughly corresponds to 1/10th of the expected Poisson noise.

To summarize, our scheme for generating a synthetic catalog of stars using the adaptive von Neumann sampling algorithm is as follows. For each node, we first determine N_{node} , the number of stars that need to be generated. Next, to assign position and age to stars, we randomly select \mathbf{r} and τ and then accept or reject them using the von Neumann scheme. Next, the mass m for a star is sampled from the IMF $\xi(m)$ and Z from $f_Z(Z, \mathbf{r}, \tau)$. The nearest isochrone corresponding to (Z, τ) is selected and the stellar parameters corresponding to m are determined. The velocities are assigned according to the distribution function $f_{\text{vel}}(\mathbf{v}, \mathbf{r}, \tau)$, which is generally in

the form of an ellipsoid or can be subjected to more advanced treatment, an issue that we revisit later. Finally, we use a selection function to decide if a star enters the final catalog of the survey. The process of spawning stars is repeated for all nodes to generate the full catalog.

During the star spawning process we do not take into account the effect of photometric errors or extinction. This is because each observational survey will have different photometric error laws, and it is not possible to formulate a general scheme for this. Also, there is no perfect 3d model for extinction. Although, we do provide a default extinction model (see Section 2.6), but a user might be interested in trying out other models too. However, photometric errors and extinction can be easily handled as a post processing step and this is the approach that we follow. To accomplish this, first, one has to generate a catalog with color magnitude ranges slightly larger than the desired ranges and then for each star add the expected extinction and subsequently the photometric errors. Finally, using these transformed magnitudes one can select the stars lying within the desired color magnitude limits.

2.3. Speeding up the star spawning process

The process of spawning stars from a node, as discussed in the previous section, can be further optimized and we discuss this below. To begin with, the distribution of stellar masses is such that there are a lot of low mass stars but very few high mass stars. Low mass stars are also low in luminosity hence for a magnitude limited survey only nearby low-mass stars are visible. On the other hand, the volume explored increases as the cube of the distance. Hence for most of the nodes the low mass stars do not enter the final catalog. We use this information to optimize our scheme — for each node we first determine the lowest stellar mass m_{\min}^{node} that can generate a visible star and then exclusively generate stars having mass above this limit. The number of stars from a node that fall into a survey is then given by

$$N_{\text{vis}}^{\text{node}}(m_{\min}^{\text{node}}, m_{\max}) = \int_{m_{\min}^{\text{node}}}^{m_{\max}} \xi(m) dm \int_{\text{node}} g(\mathbf{r}, \tau) d^3r d\tau \\ = N^{\text{node}} \xi(> m_{\min}^{\text{node}}) \quad (10)$$

We use stochastic rounding to convert $N_{\text{vis}}^{\text{node}}$ to an integer — i.e., if the fractional part of $N_{\text{vis}}^{\text{node}}$ is less than a Poisson-distributed random number with a range between 0 and 1, we increment the integral part by 1.

We now describe the procedure to calculate m_{\min}^{node} . If r is the heliocentric distance of a node, having sides of length l_{node} , then calculating m_{\min}^{node} requires computing the minimum mass of a star that will be visible at a distance $r - \sqrt{3}l_{\text{node}}$ for each isochrone and then computing the global minimum, i.e., over isochrones of all ages and metallicities. Doing this individually for each node might be computationally expensive. However, it is possible to optimize this. First, for a given galactic component, we identify the set of isochrones that have a non-zero probability of being sampled and compute m_{\min}^{node} over these set of isochrones only. Secondly, we note that for a given set of isochrones m_{\min}^{node} is a monotonically increasing function of heliocentric distance. Since, we can choose any value of m_{\min}^{node} that is smaller than the smallest visible mass, we access the nodes in a sequence sorted by their minimum heliocentric distance, $r - \sqrt{3}l_{\text{node}}$, and recompute m_{\min}^{node} whenever the distance changes by a

fixed step size (a step size of 0.1 mag in distance modulus).

2.4. Sampling an N-body model

An N-body model consists of a finite set of particles distributed in phase space (\mathbf{r}, \mathbf{v}) . Let $f_{\text{phase-space}}^{\text{N-body}}(\mathbf{r}, \mathbf{v})$ be the phase space distribution function describing this. An N-body particle in general represents a collection of stars rather than a single star. Let $m^{\text{N-body}}$ be the mass of the stellar population corresponding to the N-body particle and this represents the mass of stars that were ever formed (summed over all ages). Also let us assume the age, metallicity and mass distribution to be given by $\Psi(\tau)$, $f_Z(Z, \tau)$, and $\xi(m)$ respectively. The distributions being normalized such that $\int \Psi(\tau) f_Z(Z, \tau) \xi(m) dZ d\tau dm = 1$. The distribution function of stars is then given by

$$f^* = f_{\text{phase-space}}^{\text{N-body}}(\mathbf{r}, \mathbf{v}) \times \Psi(\tau) f_Z(Z, \tau) \xi(m) m^{\text{N-body}} / \langle m \rangle \quad (11)$$

where the simulations provide the spatial and kinematic behavior represented by the phase space density term $f_{\text{phase-space}}^{\text{N-body}}(\mathbf{r}, \mathbf{v})$.

For an N-body model, the fact that the number of N-body particles is finite leads to the following problem — if the number density of visible stars at a given point in space is more than the number density of N-body particles at the same point one needs to oversample the particles. The condition for this is given by

$$\int d\tau dZ \int_{m_{\min}(r)}^{m_{\max}} f^* dm > f_{\text{phase-space}}^{\text{N-body}}(\mathbf{r}, \mathbf{v}),$$

or in other words

$$\xi(> m_{\min}(r)) \frac{m^{\text{N-body}}}{\langle m \rangle} > 1, \quad (12)$$

$m_{\min}(r)$ being the minimum mass of a star that is visible at a heliocentric distance of r . Typically such a situation arises when r is small, i.e., in regions close to the sun. Hence unless one simulates the N-body model with the number of particles equal to the number of stars in the model galaxy, one has to live with oversampling. The question now is how are we to assign positions and velocities to the oversampled particles?

The positions of oversampled particles should be assigned in such a way that they preserve the underlying phase space density. For this we first review a popular scheme of density estimation known as the kernel density estimation, which is also statistically quite robust. In this scheme the number density at a given point \mathbf{x} for an N-body system of particles is given by

$$f(\mathbf{x}) = \sum_j \frac{1}{h_j^n} K\left(\frac{r_j}{h_j}\right) \quad (13)$$

where $K(u)$ is a kernel function such that its integral over all space is unity, r_j is the distance of the j -th particle from \mathbf{x} , and n the dimensionality of the space. In a multivariate setting, r_j is given by

$$r_j = \sqrt{(\mathbf{x} - \mathbf{x}_j)^T \Sigma_j^{-1} (\mathbf{x} - \mathbf{x}_j)} \quad (14)$$

where Σ_j^{-1} is the matrix representing the distance metric and is normalized such that $\det(\Sigma_j) = 1$. The smoothing length

TABLE 1
GEOMETRY OF STELLAR COMPONENTS. THE FORMULAS USED ARE FROM ROBIN ET AL. (2003). NOTE, (R, θ, z) ARE THE COORDINATES IN THE GALACTOCENTRIC CYLINDRICAL COORDINATE SYSTEM AND $a^2 = R^2 + \frac{z-z_{\text{warp}}}{k_{\text{flare}}\epsilon(\tau)}$ (FOR THE THIN DISC).

Component	Age (Gyr)	density law $\rho(\mathbf{r}, \tau)$
Thin Disc	≤ 0.15	$\frac{\rho_c \Psi(\tau)}{k_{\text{flare}} \epsilon(\tau)} \{ \exp(-(a/h_{R+})^2) - \exp(-(a/h_{R-})^2) \}$ where: $h_{R+} = 5000$ pc, $h_{R-} = 3000$ pc IMF- $\xi(m) \propto m^{-1.6}$ for $m < 1 M_{\odot}$ and $\xi(m) \propto m^{-3.0}$ for $m > 1 M_{\odot}$
Thin Disc	0.15–10	$\frac{\rho_c \Psi(\tau)}{k_{\text{flare}} \epsilon(\tau)} \{ \exp(-(0.5^2 + \frac{a^2}{h_{R+}^2})) - \exp(-(0.5^2 + \frac{a^2}{h_{R-}^2})) \}$ where: $h_{R+} = 2530$ pc, $h_{R-} = 1320$ pc, IMF- $\xi(m) \propto m^{-1.6}$ for $m < 1 M_{\odot}$ and $\xi(m) \propto m^{-3.0}$ for $m > 1 M_{\odot}$
Thick disc	11	if $ z \leq x_l$, $\rho_c \delta(\tau - 11) \exp(-\frac{R-R_{\odot}}{h_R}) \times (1 - \frac{1/h_z}{x_l \times (2+x_l/h_z)} \times z^2)$ if $ z > x_l$, $\rho_c \delta(\tau - 11) \exp(-\frac{R-R_{\odot}}{h_R}) \times \frac{\exp(x_l/h_z)}{1+x_l/2h_z} \exp(-\frac{ z }{h_z})$ where: $h_R = 2500$ pc, $h_z = 800$ pc, $x_l = 400$ pc IMF- $\xi(m) \propto m^{-0.5}$
Spheroid	14	$\rho_c \delta(\tau - 14) \left(\frac{\text{Max}(a_c, a)}{R_{\odot}} \right)^{n_H}$ where: $a^2 = R^2 + \frac{z^2}{\epsilon^2}$, $a_c = 500$ pc, $\epsilon = 0.64$, $n_H = -2.77$ IMF- $\xi(m) \propto m^{-0.5}$
Bulge	10	if $\sqrt{x^2 + y^2} < R_c$, $\rho_c \delta(\tau - 10) \exp(-0.5r_s^2)$ if $\sqrt{x^2 + y^2} > R_c$, $\rho_c \delta(\tau - 10) \exp(-0.5r_s^2) \times \exp(-0.5(\frac{\sqrt{x^2 + y^2} - R_c}{0.5})^2)$ where: $r_s^2 = \sqrt{[(\frac{x}{x_0})^2 + (\frac{y}{y_0})^2]^2 + (\frac{z}{z_0})^4}$, $R_c = 2.54$, $x_0 = 1.59$, $y_0 = z_0 = 0.424$, $\alpha = 78.9^\circ$, $\beta = 3.5^\circ$, $\gamma = 91.3^\circ$ IMF- $\xi(m) \propto m^{-2.35}$
ISM		$\rho_c \exp(-\frac{R-R_{\odot}}{h_R}) \times \exp(-\frac{ z }{h_z})$ where: $h_R = 4500$ pc, $h_z = 140$ pc
Dark halo		$\frac{\rho_c}{(1+(a/R_c)^2)}$ where: $R_c = 2697$ pc and $\rho_c = 0.1079$

h of a particle is determined as the distance to the k -th nearest neighbor from the location of the particle. The physical interpretation of the density scheme is that if each point is assumed to be a hyper-ellipsoidal ball with mass distributed according to the kernel function K and having a covariance of $h^2 \Sigma$, then the underlying smooth density field is simply the result of superposition of such balls. This suggests that if the spawned stars are also distributed around the particle in a similar fashion, i.e., distributed according to the kernel function K and having a covariance is $h^2 \Sigma$, then they will essentially be sampling the density field of the N-body system.

The question that remains is how to determine the optimum covariance matrix Σ ? The simplest scheme is to use a global metric based on the variance of the data along each dimension. A global metric, however, is insufficient for accurately calculating the phase space densities. What is needed is a locally adaptive metric that changes with the local configuration of the data at each point in space (Sharma & Steinmetz 2006; Sharma & Johnston 2009). Such a metric can be calculated using the publicly available multidimensional density estimation code EnBiD by Sharma & Steinmetz (2006). EnBiD, which is an improvement over a scheme proposed by Ascasibar & Binney (2005), makes use of a binary space partitioning scheme along with the use of the information theoretic concept of Shannon entropy to handle the issue of determining the optimal locally adaptive distance metric Σ_j^{-1} in a multi-dimensional space. For our use, we adopt the En-

BiD scheme with the number of nearest neighbors k set to 64, which we find is adequate for reproducing a smooth distribution of stars in the phase space. Too small a value leads to lumpiness around the N-body particles and too large a value erodes the positional accuracy of the data. We assume the matrix Σ to be diagonal and use the cubic cell scheme of EnBiD, i.e. $\Sigma_{11} = \Sigma_{22} = \Sigma_{33}$ and $\Sigma_{44} = \Sigma_{55} = \Sigma_{66}$ (dimensions 1,2 and 3 representing position coordinates while the dimensions 4,5 and 6 the velocity coordinates). The EnBiD algorithm was applied individually to each of the disrupted satellites in the simulations.

In order to assess the usefulness of EnBiD for our particular application, we plot in Figure 1 (lower right panel) the distribution of the velocity scale factor $\sqrt{\Sigma_{11}/\Sigma_{44}}$, which is the ratio of position to velocity scale and has units of kpc/km s $^{-1}$, as estimated by EnBiD for the N-body particles from one of the simulations of a disrupted satellites by Bullock & Johnston (2005) (see Section 3.4). It can be seen that the scale factor varies by about 3 orders of magnitude, which demonstrates the inappropriateness of a global metric and the need for a locally adaptive metric scheme. The huge variation is due to the fact that during phase mixing the phase space density of particles is approximately conserved. This means that high density regions in position space will correspond to low density regions in velocity space and vice versa. This can be easily seen in the panels of Figure 1, where scatter plots of particles in position and velocity space has been

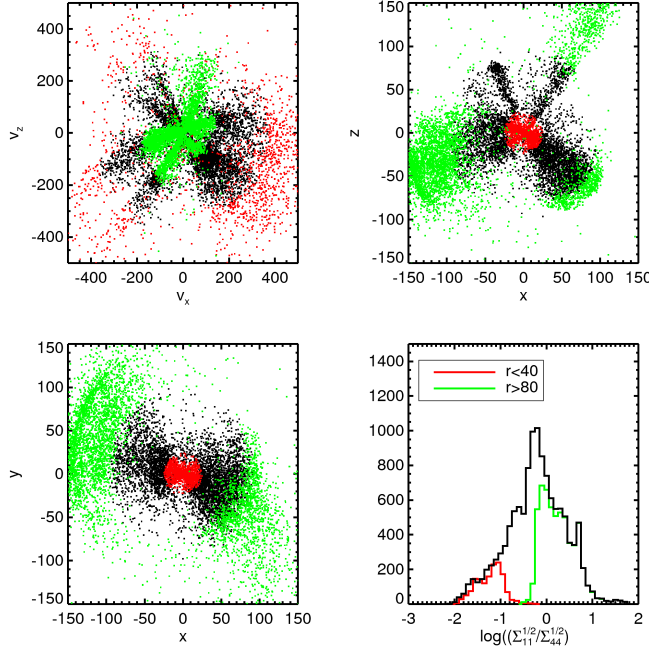


FIG. 1.— Distribution of the velocity scale factor in units of $\text{kpc}/\text{km s}^{-1}$ for one of the disrupted satellites from BJ05 simulations and its dependence on location in phase space. The bottom left panel shows the distribution of velocity scale factor while the other panels show the scatter plot of particles in position and velocity space. The particles lying in the inner ($r < 40$) and outer regions ($r > 80$) of the halo are colored red and green respectively (r being the radial distance from the center of the stellar halo). High density regions in position space are low density regions in velocity space and vice versa.

shown. The high density regions in position space ($r < 40$) are colored red while the low density regions in position space ($r > 80$) are colored green. The mean value of scale factor $\langle \sqrt{\Sigma_{11}/\Sigma_{44}} \rangle$ was found to be 0.057 and 2.9 for the red and green regions (see lower right panel for distributions). As a check we computed the scale factor using variance of the particles $\sqrt{(\sigma_x^2 + \sigma_y^2 + \sigma_z^2)/(\sigma_{v_x}^2 + \sigma_{v_y}^2 + \sigma_{v_z}^2)}$. The values obtained were 0.037 and 2.3 for red and green particles respectively, which are in agreement with results reported by EnBiD.

Summarizing, the scheme for sampling N-body distributions is as follows. Select a particle i , determine if the dispersing volume, defined by the kernel function K and the smoothing length h_i , intersects with the survey volume, and calculate the number of visible stars it spawns, i.e., $N_{\text{vis}}^i = m^{\text{N-body}} \xi(> m_{\text{min}}(r))/\langle m \rangle$. We use stochastic rounding as discussed earlier to convert N_{vis}^i to an integer. Next, for each spawned star we generate τ , Z and m according to the distribution functions Ψ_τ , $f_Z(Z, \tau)$ and $\xi(m)$ and disperse them in phase space using the scheme discussed above. Finally, we use a selection function to decide if a star enters the final catalog of the survey.

2.4.1. Improving the positional accuracy while sampling an N-body model

Dispersing the stars spawned by an N-body particle in phase space has its side effects. This adds noise to the data, the effect of which is to reduce the positional accuracy. When a particle is oversampled one cannot avoid the noise but when a particle is under-sampled or equally-sampled i.e., less than

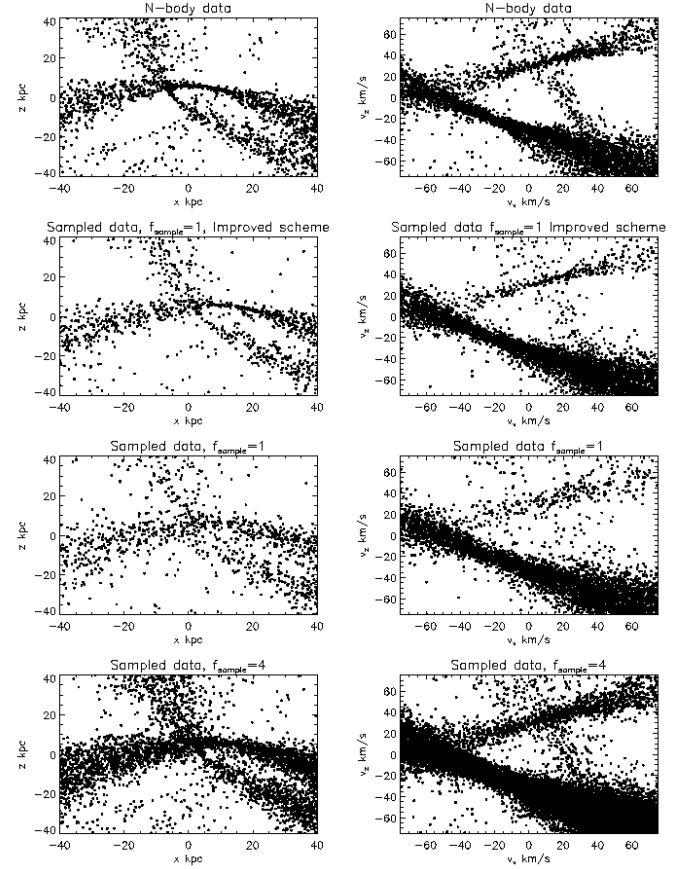


FIG. 2.— Position and velocity scatter plots of a disrupted satellite sampled from an N-body simulation of Bullock & Johnston (2005). The upper panels show the original N-body data while the rest of them are for sampled data. The sampling fraction f_{sample} is labeled on the panels. The panels in second row use an improved scheme that disperses the spawned stars in phase space only when more than one star is spawned by an N-body particle. Note, the stellar mass associated with an N-body particle is not necessarily constant.

or equal to one star needs to be spawned from the N-body particle, one can eliminate the noise by simply assigning the coordinates of the particle directly to the spawned star. But it is not possible to know a priori as to how many stars from a particle will enter final catalog. To overcome this we implement a scheme which makes sure that, among the stars spawned by a particle if one of the stars can be reassigned the coordinates of its parent particle without it being excluded from the final catalog we do so. The effect of this improved sampling scheme is shown in Figure 2 which shows the position (left panels) and velocity (right panels) scatter plot of a disrupted satellite system from an N-body simulation of Bullock & Johnston (2005). The panels in the top row show the N-body particles in the simulation, while the other rows show the stars sampled from it. The sampling fraction f_{sample} , i.e., average number of spawned stars per N-body particle, is also labeled on each of the panels. For illustrative purpose we assume the number of stars spawned per unit mass of the particle to be constant but in a realistic simulation it will depend upon the heliocentric distance of the particle. First, we compare the first row with the second row that shows the results of the improved scheme for the case of $f_{\text{sample}} = 1$. The distribution of position coordinates is nearly identical for both rows which is what we expect when $f_{\text{sample}} = 1$. On closer scrutiny, in some regions a loss of positional accuracy can be

seen. Also some regions apparently seem to be undersampled. This departure from the ideal behavior is because the stellar mass associated with an N-body particle obtained from the simulations that we use, is not necessarily constant. So some N-body particles can spawn more than one star which subsequently needs to be dispersed in phase space. Next, we compare the results of the improved scheme (second row) with the naive scheme (third row) that disperses all stars for the same value of $f_{\text{sample}} = 1$. It can be clearly seen that the improved scheme has better positional accuracy. For reference, the last row shows the case of $f_{\text{sample}} = 4$. We revisit this issue in Section 5.2 and Section 5.3 and discuss in greater detail the consequences of our scattering scheme for real applications.

2.5. Stellar Isochrones

Theoretical stellar isochrones are one of the main ingredients of our scheme. These are used to assign parameters like luminosity, effective temperature, magnitude and color to a star of a given age, metallicity and mass. We employ Padova isochrones (Marigo et al. 2008; Marigo & Girardi 2007; Girardi et al. 2000; Bertelli et al. 1994), which are available for a wide variety of photometric systems² and unlike other popular isochrones also cover the asymptotic giant branch and the red clump phases of stellar evolution.

We now describe the scheme for interpolating across different isochrones. An isochrone, for a given age and metallicity, is a table of stellar parameters, e.g., magnitudes, effective temperature and gravity, as a function of stellar mass. Hence in a given isochrone, stellar parameters for any intermediate mass can be easily computed by linear interpolation. However, interpolating across isochrones of different ages and metallicities involves the use of equivalent evolutionary points, which are not always provided with the isochrones. Hence, for the sake of flexibility as well as computational ease we adopt a simpler scheme. To begin with, a grid of 182×34 isochrones spanning an age interval of $6.6 < \log t/\text{yr} < 10.22$ (step size of $\Delta \log(t) = 0.02$) and metallicity interval of $10^{-4} < Z < 3 \times 10^{-2}$ (mean step size of $\Delta \log(Z) \sim 0.072$) were chosen. Next, for a star of a given age and metallicity, the nearest isochrone in the grid was identified. Subsequently, this isochrone was used to compute the stellar parameters by linear interpolation in mass. Where needed, the metallicity Z was converted to $[\text{Fe}/\text{H}]$ using the relation

$$[\text{Fe}/\text{H}] = \log(Z/Z_{\odot}); \text{ where } Z_{\odot} = 0.019 \quad (15)$$

In the above mentioned scheme, to simulate the color magnitude diagrams accurately, the adopted grid should have a fine enough resolution; and our adopted resolution was found to be adequate for this purpose. However, for greater accuracy if desired one can increase the resolution of the grid.

The Padova isochrones are limited to stellar masses greater than $0.15 M_{\odot}$. For lower masses extending up to the hydrogen mass burning limit ($0.07 M_{\odot} < m < 0.15 M_{\odot}$) we use the isochrones from Chabrier et al. (2000). Since, these isochrones are only available for solar metallicity, we used them for all metallicities. Also, the Chabrier et al. (2000) isochrones are only available for Johnson-Cousin bands, hence, in order to be able to support a variety of photometric bands, we choose to compute absolute magnitudes for the above mentioned low

mass stars using the bolometric correction (BC) tables from <http://stev.oapd.inaf.it/dustyAGB07/>, which is a database of BC tables for different photometric bands provided by the Padova group (Marigo et al. 2008; Girardi et al. 2002, 2004).

Note, in the present version of the code we do not model the white dwarfs. White dwarfs are quite faint ($M_V > 10$) and rare compared to other type of stars and hence for most applications they do not dominate the star counts. However, in applications where one expects to find white dwarfs caution should be exercised when interpreting the results of *Galaxia*.

2.6. Extinction

Most stellar observations suffer from extinction by dust and this needs to be taken into account when comparing simulated catalogs with stellar surveys. Although the total extinction along a given line of sight has been accurately mapped (Schlegel et al. 1998), the same cannot be said for the 3D distribution of dust. Drimmel et al. (2003) provide a sophisticated model for the 3D dust distribution, and other alternatives include Marshall et al. (2006). Since a comprehensive extinction model is beyond the scope of this paper, we provide here only a simple extinction correction scheme. Note, extinction is basically a post processing step and once an extinction-free catalog has been generated using *Galaxia*, one can subject it to the extinction model of one's choice.

The extinction scheme we use is a refinement of the method proposed by Bland-Hawthorn et al. (2010b). The 3D distribution of the dust is modeled as a double exponential disc,

$$\rho_{\text{Dust}}(R, z) = \frac{\rho_0}{k_{\text{flare}}} \exp\left(-\frac{R - R_{\odot}}{h_R}\right) \times \exp\left(-\frac{|z - z_{\text{warp}}|}{k_{\text{flare}} h_z}\right). \quad (16)$$

where $z_{\text{warp}}(R, \phi)$ and $k_{\text{flare}}(R)$ describe the warp and flare of the disc and are described in Section 3.2. The values of the parameters controlling the warp and flare were assumed to be same as that of the stellar disc. Next, we use the Schlegel et al. (1998) $E(B - V)$ dust maps to evaluate the best fit parameters of the dust model and obtained $h_R = 4200$ pc, $h_z = 88$ pc and $\rho_0 = 0.54 \text{ mag/kpc}$. The fit parameters were obtained by minimizing

$$\chi^2 = \sum \left(\frac{E_i^{\text{map}} - E_i^{\text{model}}}{E_i^{\text{map}}} \right)^2 \quad (17)$$

where $E_i^{\text{model}} = \int_0^{\infty} \rho_{\text{Dust}}(l_i, b_i, r) dr$ is the extinction in the cell i defined in the (l, b) space. The fit was performed in the range $-15^\circ < b < 15^\circ$ assuming $R_{\odot} = 8.0$ which defines the distance scale.

The modeled dust disc is then used to generate a 3D extinction map in galactic coordinates l, b and r , by integrating the dust density along different lines of sight. The angular resolution of the 3D maps was assumed to be 1024×1024 while in the radial directions 512 logarithmically spaced bins in the range $0.01 < r < 30$ kpc were used. Values for any arbitrary position were obtained from the maps by linear interpolation in (r, l, b) . Alternately, one can also assume a directional dependent normalization constant ρ_0 such that the total extinction at infinity along a given line of sight equals the value in the Schlegel et al. (1998) maps. For this we use high resolution Schlegel et al. (1998) maps having an angular resolution of 4096×4096 in l and b . We employ this as our default scheme.

² The isochrones were downloaded from <http://stev.oapd.inaf.it/cgi-bin/cmd>

TABLE 2
AGE AND METALLICITY DISTRIBUTION (MEAN AND DISPERSION) OF
GALACTIC COMPONENTS. THE VALUES SHOWN ARE FROM
ROBIN ET AL. (2003)

	Age (Gyr)	[Fe/H]	$\sigma_{[\text{Fe}/\text{H}]}$	$d[\text{Fe}/\text{H}]/dR$
Thin disc	0-0.15	-0.01	0.12	
	0.15-1	-0.03	0.12	
	1-2	-0.03	0.10	
	2-3	-0.01	0.11	-0.07
	3-5	-0.07	0.18	
	5-7	-0.14	0.17	
	7-10	-0.37	0.20	
Thick disc	11	-0.78	0.30	0
Stellar Halo	14	-1.78	0.50	0
Bulge	10	0.00	0.40	0

Note, Schlegel extinction maps are known to overestimate the extinction in the Galactic plane (regions where $A_V > 0.5$ mag), by about 30% (Arce & Goodman 1999; Cambr sy et al. 2005). While Arce & Goodman (1999) report results in a strip of few degrees in length only, Cambr sy et al. (2005) report mean values in galactic anti-center hemisphere only. Since a proper recalibrated map is not yet available it is difficult to take these effects into account. In addition to directly affecting the total value of extinction along a particular line of sight, the overestimation is also expected to affect the determination of our scale height for the dust disc, which in turn will affect the variation of extinction with distance. If we assume the overestimation factor to be a monotononic function of extinction we expect the actual scale height of the dust disc to be larger than what we find here. Hence, we advise caution to be exercised when using our extinction scheme in the galactic plane.

3. A WORKING MODEL OF THE GALACTIC COMPONENTS

The main ingredients of our galactic model as described by Equation (2) are the star formation rate (SFR), the age velocity relation (AVR), the IMF and the density profiles. We now discuss the adopted functional forms for each of these functions so as to arrive at a working model of the Galaxy. Instead of doing a detailed modeling we here implement the well known and well tested Besan on model. The density distributions and the ages and metallicity of various galactic components are given in Table 1 and Table 2, these are the same as the one used by Robin et al. (2003) (R03 hereafter). The thin disc spans an age interval of 0 – 10 Gyr. On the other hand, the thick disc, the bulge and the halo are all assumed to have a constant age.

3.1. Thin and thick disc

In the Besan on model, the axis ratio ϵ and velocity dispersions σ_R , σ_ϕ and σ_z , for the thin disc, are tabulated as a function of age τ (velocity ellipsoid being taken from Gomez et al. (1997). Here we parameterize them as functions. The axis ratio ϵ is parameterized as

$$\epsilon(\tau) = \text{Min} \left(0.0791, 0.104 \left(\frac{\tau + \tau_{\min}}{\tau_{\max} + \tau_{\min}} \right)^{0.5} \right), \quad (18)$$

and for velocity dispersions we use Equation (6). To match the Besan on values, the velocity dispersion for the thin disc is assumed to saturate at $0.862\sigma_{R0,\phi0,z0}$ and a value of $\tau_{\max} = 10.0$ and $\tau_{\min} = 0.1$ is used. The values of parameters used are summarized in Table 3. The adopted values

TABLE 3
VELOCITY ELLIPSOID OF STELLAR COMPONENTS. NOTE, (R, ϕ, z) ARE
THE COORDINATES IN THE GALACTOCENTRIC CYLINDRICAL
COORDINATE SYSTEM.

	σ_{R0} kms/s	$\sigma_{\phi0}$ kms/s	σ_{z0} kms/s	q	β
Thin disc	50	32.3	21	0.33	0.33
Thick disc	67	51	42	0.33	0.33
Spheroid	141	75	75	0	0
Bulge	110	110	100	0	0

for the thin and thick disc reproduce the Besan on results. Note, the radial dependence of velocity dispersions is modeled here using Equation (6) (values of q and β being from Sch nrich & Binney 2009), rather than the Besan on model that assumes $d \ln \sigma_R^2/dR = -0.2 \text{ kpc}^{-1}$ and zero derivative for other components. Note, the circular velocity profile is computed from the Besan on mass model and at the location of the Sun it has a value of 226.84 km s^{-1} .

3.2. Warp and flare

The thin and thick discs are assumed to have a warp and a flare that is modeled following the prescription of R03. Assuming galactocentric cylindrical coordinates (R, ϕ, z) , stars with radius $R > R_{\text{warp}}$ are displaced perpendicular to the plane by an amount

$$z_{\text{warp}}(R, \phi) = \gamma_{\text{warp}} \text{Min}(R_{\text{warp}}, R - R_{\text{warp}}) \cos(\phi - \phi_{\max}) \quad (19)$$

where ϕ_{\max} is the direction in which the warp is maximum. For flaring, stars with $R > R_{\text{flare}}$ have their scale heights increased by a factor

$$k_{\text{flare}}(R) = 1 + \gamma_{\text{flare}} \text{Min}(R_{\text{flare}}, R - R_{\text{flare}}) \quad (20)$$

For the parameters we adopt the same values as that used by R03, namely $\phi_{\max} = 90.0$, $\gamma_{\text{warp}} = 0.18 \text{ kpc}^{-1}$, $R_{\text{flare}} = 1.12 R_\odot$ and $\gamma_{\text{flare}} = 0.0054 \text{ kpc}^{-1}$.

3.3. Bulge

It has been well established that the Milky Way hosts a bar-shaped bulge (Blitz 1993). With the arrival of the COBE infrared maps, it has been possible to construct 3d models to fit the data. Various models using different triaxial analytic functions were presented by Dwek et al. (1995), of which the G2 model (boxy triaxial Gaussian type functions) provided the best fit to the data. The G2 bar is used by the Besan on model and is adopted by us in our initial demonstration of the *Galaxia* model. The G2 density distribution has a core at the center defined by radius R_c and the distribution is elongated along one axis which defines the major axis. The orientation of the major axis is defined by three angles α , β and γ . The values for these parameters are taken from R03, where they obtained the values by fitting the model to the near infrared star counts of the DENIS survey.

Next, we describe the kinematic properties of our model. Self-consistent dynamical models have been presented that use either the Schwarzschild technique Zhao (1996) or are extracted from N-body simulations (Fux 1999; Athanassoula & Misiriotis 2002), but these are beyond the scope of the current paper. Instead, we attempt to create a simple working model that roughly satisfies the existing observational data and would be useful for studying the systematic effects that cloud the interpretation of observation data.

A number of earlier studies have claimed that the bulge is in solid body rotation by fitting a straight line to the plot of mean radial velocity as a function of longitude (also referred to as a rotation curve), e.g., by Menzies (1990) using Mira variables and by Izumiura et al. (1995) using SiO maser stars. A slope of about $10 \text{ km s}^{-1} \text{ deg}^{-1}$ has generally been reported, which translates to a pattern speed of $\Omega = 71.62 \text{ km s}^{-1} \text{ kpc}^{-1}$, assuming 8 kpc as the distance to the galactic center. Recently, Howard et al. (2009) have also measured the rotation curve using bulge M-giants in two strips at $b = -4$ and $b = -8$. They report the two rotation curves to be nearly identical, suggesting that the bulge is rotating cylindrically. A straight line fit (by eye) to their rotation curve also seems to suggest a value close to $10 \text{ km s}^{-1} \text{ deg}^{-1}$. Hence, for simplicity we adopt the value of $\Omega = 71.62 \text{ km s}^{-1} \text{ kpc}^{-1}$ for the pattern speed of the bulge. Note, Howard et al. (2008) also report that the rotation curve for the $b = -4$ strip, shows evidence of flattening beyond $|l| > 4$.

Having specified the rotation we next review the velocity dispersions. Specifically, we attempt to fix the values for the velocity dispersions σ_R , σ_ϕ and σ_z of our model, expressed in cylindrical coordinates with respect to the galactic center. A value of $\sigma_r = 110.0 \text{ km s}^{-1}$ has typically been reported for the line of sight velocity dispersion in Baade's window (Terndrup et al. 1995; Binney & Merrifield 1998) and this is what we assume for σ_R . Recent results by Howard et al. (2009, 2008) also confirm this but show a variation with both latitude and longitude— at $b = -4$, σ_r is found to increase from 70 km s^{-1} to 110 km s^{-1} with $|l|$ varying from 10° to 0° , while at $b = -8$, σ_r is found to be relatively constant with a value of 70 km s^{-1} .

Using proper motions, velocity dispersions along l and b have also been measured and an anisotropy of $\sigma_l/\sigma_b = 1.15$ has been reported (Rattenbury et al. 2007; Vieira et al. 2007; Spaenhauer et al. 1992). The anisotropy could both be due to intrinsic anisotropy as well as due to the rotational broadening as demonstrated by Zhao et al. (1996). Since it is not possible to exactly deduce the value of σ_ϕ from σ_l we assume for simplicity $\sigma_\phi = \sigma_R$ and choose the value of σ_z so as to reproduce the observed value of anisotropy ratio in Baades's window. For a choice of $\sigma_z = 100 \text{ km s}^{-1}$, the bulge stars lying in the field $(l, b) = (1^\circ, -4^\circ)$ and with heliocentric distance between 7–9 kpc, were found to have $\sigma_l/\sigma_b = 1.17$.

3.4. Simulated stellar halo

To make theoretical predictions of structures in the stellar halo, we use the eleven stellar halo models of Bullock & Johnston (2005), which were simulated within the context of the Λ CDM cosmological paradigm. These simulations follow the accretion of individual satellites modeled as N -body particle systems onto a galaxy whose disc, bulge, and halo potential is represented by time dependent analytical functions. Semi-analytical prescriptions are used to assign a star formation history to each satellite and a leaky accreting box, chemical enrichment model is used to calculate the metallicity as a function of age for the stellar populations (Robertson et al. 2005; Font et al. 2006). The dark matter halos are assumed to follow an NFW density profile whereas, the stellar matter is assumed to follow a Kings profile embedded within the dark matter halos. To simulate Kings profile within dark matter profiles the dark matter particles are assigned a stellar mass which is a function of the energy of the

dark matter particles³. The stellar masses depend upon the adopted star formation time scale and the later is chosen by requiring that the simulated satellite stellar distributions reproduce the structural properties of Local Group dwarf galaxies. The three main model parameters of an accreting satellite are the time since accretion, t_{acc} , its luminosity, L_{sat} , and the circularity of its orbit, defined as $\epsilon = J/J_{\text{circ}}$ (J being the angular momentum of the orbit and J_{circ} the angular momentum of a circular orbit having same energy). The distribution of these three parameters describes the accretion history of a halo. To study the sensitivity of the properties of structures in the stellar halo to accretion history, additionally a set of six artificial stellar halo models (referred to as non- Λ CDM halos) were generated by Johnston et al. (2008). These have accretion events that are predominantly (i) *radial* ($\epsilon < 0.2$), (ii) *circular* ($\epsilon > 0.7$), (iii) *old* ($t_{\text{acc}} > 11 \text{ Gyr}$), (iv) *young* ($t_{\text{acc}} < 8 \text{ Gyr}$), (v) *high-luminosity* ($L_{\text{sat}} > 10^7 L_\odot$), and (vi) *low-luminosity* ($L_{\text{sat}} < 10^7 L_\odot$).

3.5. Analytic smooth stellar halo

For some applications it is also necessary to have a smooth stellar halo. We do this by assuming an oblate power law distribution with ellipticity $\epsilon = 0.76$ and power law index of $n_H = -2.44$ as suggested by R03. The values of ϵ and n_H can be altered if desired, e.g., recent results by Jurić et al. (2008) using SDSS predict a flatter halo ($\epsilon = 0.64$) and steeper value for the power law index ($n_H = -2.77$). In accordance with the results of Bond et al. (2010), the principal axes of the velocity ellipsoid are assumed to be aligned with a spherical coordinate system and the velocity dispersions are assumed to be $\sigma_r = 141 \text{ km s}^{-1}$ and $\sigma_\theta = \sigma_\phi = 75 \text{ km s}^{-1}$. The spheroid is assumed to have no net rotation.

3.6. Initial mass function and normalizations

Having specified the density functions, we now provide the the initial mass function ξ and the normalization constants like ρ_c and the star formation rate $\Psi(\tau)$. As in the Besançon model, the IMF was assumed to be of a power law form, $\xi(m) = m^{-\alpha}$, the values of α are tabulated in Table 1. The mass limits of the IMF were defined to be in the range $0.07 < m < 100$. Next, the density normalization constants were chosen to reproduce the local mass density of current stars ρ_0 for the various galactic components in the solar neighborhood (Table 2 in R03). This resulted in a star formation rate of $\Psi = 2.85 M_\odot/\text{yr}$ and ρ_c of 1.55×10^9 and $1.31 \times 10^7 M_\odot \text{ kpc}^{-3}$ for the thick disc and the stellar halo respectively. However, for the thin disc in the regime $7 < \tau < 10 \text{ Gyr}$ the SFR had to be lowered by 20% in order to match the star counts in the Besançon model. This is because in this regime the isochrones employed by us differ from those in the Besançon model. For the bulge $\rho_c = 3.49 \times 10^9 M_\odot \text{ kpc}^{-3}$ was selected which gives a central density of $13.76 \text{ stars pc}^{-3}$ in accordance with the Besançon model.

For our analysis, we assume the Sun to be located at a radial distance of 8 kpc from the center of the galaxy (Eisenhauer et al. 2003; Reid 1993) Since our adopted radial distance of Sun is different from the Besançon model (8.5 kpc), we need to recompute the SFR. The re-calibrated value of SFR for our adopted location of the Sun turns out to

³ We actually use the massless test particles which have 10 times the phase space resolution of the original dark matter particle (see Bullock & Johnston (2005) for further details).

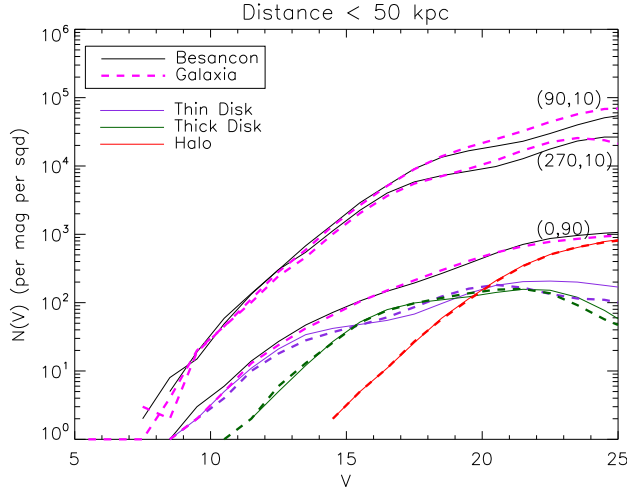


FIG. 3.— Star count predictions of *Galaxia* in various directions compared with those of the Besançon model. For the direction along the North pole the contributions for different galactic components are shown separately.

be $2.37 M_{\odot}/\text{yr}$. Also, to match the star counts for the stellar halo at large distances (along the north galactic pole) with those of the Besançon model, we had to increase the local mass density of the stellar halo by 10%.

4. TESTS AND RESULTS

In this section we test the code by comparing its predictions with various observational constraints.

4.1. Comparison with Besançon

The star count predictions of the Besançon model have been tested against a variety of observations, and since *Galaxia* uses the same disc model, it suffices for most situations to show that *Galaxia* reproduces the Besançon model. In order to keep the test simple dust extinction was neglected. To test the correspondence of our results with that of Besançon, we plot in Figure 3 the star counts as a function V band magnitude along three directions; the north galactic pole, $(l, b) = (90^{\circ}, 10.0^{\circ})$ and $(l, b) = (270^{\circ}, 10.0^{\circ})$. The last two directions were chosen to illustrate the effect of warping which results in a bifurcation in the star counts at fainter magnitudes. Overall we find good agreement with the curves from *Galaxia* corresponding closely to the Besançon curves.

For the direction along the galactic pole, the star counts for each of the galactic components are also shown separately. It can be seen that the thick disc and the stellar halo are in perfect agreement but the thin disc shows some subtle differences. For the *Galaxia* thin disc, there is a slight excess of intermediate magnitude stars and a shortage of extremely faint magnitude stars. This same effect can be seen in the other two directions also but is shifted to even fainter magnitudes. These discrepancies are due to the differences in the isochrones employed by us as compared to those used by R03. Specifically for the thin disc in the mass range $0.15 < m < 0.6$, the absolute magnitude of stars predicted by the Padova isochrones were found to be brighter than that of the isochrones used by the Besançon model.

4.2. Comparison with the Hipparcos data

The predictions of stellar properties in the solar neighborhood is an essential test for any galactic model. For these

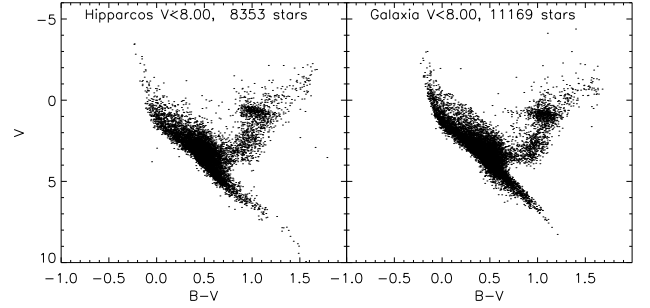


FIG. 4.— Comparison of color-magnitude diagram obtained from the Hipparcos catalog (left panel) with that of simulation from *Galaxia* (right panel). The plots show stars in the solar neighborhood defined by $V < 8$ and distance $r < 100$ pc.

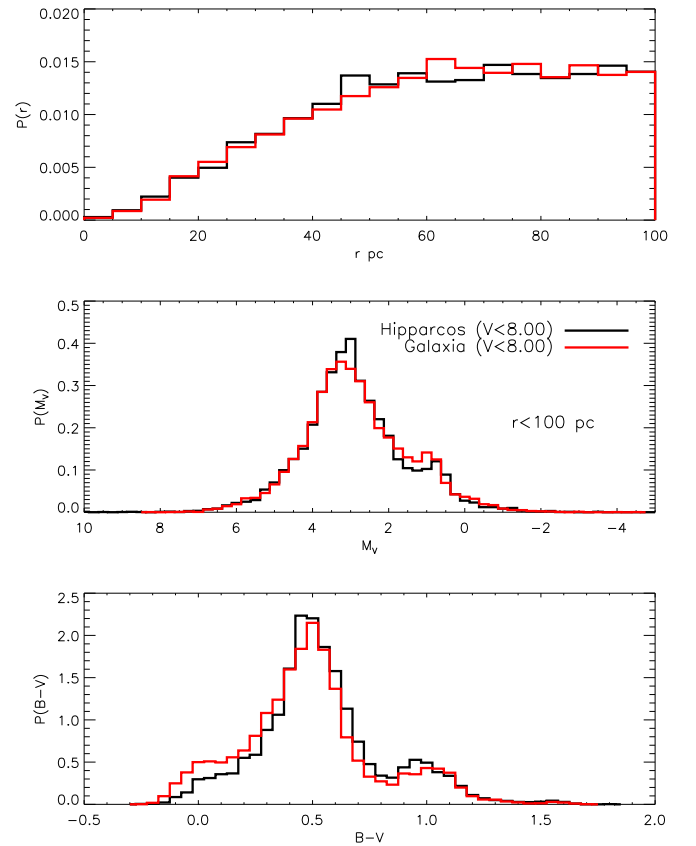


FIG. 5.— Comparison of distributions of radial distance, absolute magnitude and color for stars obtained from the Hipparcos catalog with that of simulation from *Galaxia*.

stars, accurate distances can be obtained, which enables the construction of the color-absolute magnitude diagram of stars. The Hipparcos mission (ESA 1997) produced an astrometric data base of 117955 stars down to a limiting magnitude of $V \sim 12.4$. For stars with $V < 9$, the data have a median precision of about 1 mas which is ideal for analyzing the solar neighborhood. The completeness limit of the Hipparcos catalog is estimated to be between 7.3-9 mag in V band. Hence we use the following criterion to extract a volume complete sample from the Hipparcos catalog (van Leeuwen 2007, new reduction) — $V < 8$ and parallax $\pi > 10$ mas. Binary stars were excluded from the analysis. The Hipparcos magnitude,

H_P , was converted to V band magnitude using the relation $H_P = V + 0.408(B - V) - 0.13(B - V)^2$ from Turon et al. (1992). Next, we use *Galaxia* to generate a similar catalog. The parallax errors for Hipparcos, which are a function of apparent magnitude, were simulated as in Girardi et al. (2005), where such an analysis was earlier performed. Although, Girardi et al. (2005) had not taken extinction into account we here do take it into account. For this study we adopt the extinction model presented in (Aumer & Binney 2009) such that,

$$E(B - V) = \text{Max}(0, 0.47(d - 0.07 \text{ kpc})), \quad (21)$$

which takes into account the fact that the extinction within 70 pc from the Sun is negligible. The reddening was converted to extinction assuming an R_V of 3.1. Note, the extinction is quite small, and hence it is not expected to have any significant impact on the results.

Figure 4 shows the color magnitude distribution of stars within 100 pc from the Sun using the Hipparcos and the simulated data sets. The plots are very similar. In Figure 5 the probability distributions of absolute magnitude, color and distance are also shown. All of the distributions show good agreement with the Hipparcos data. Some minor differences do exist, in particular: (i) In the radial distribution of stars there is a slight excess of stars at $r = 45$ pc and this is due to the Hyades cluster as pointed out by Girardi et al. (2005). However, unlike Girardi et al. (2005) our overall radial distribution is in good agreement with Hipparcos and does not show a deficit at low r and excess at high r as reported by them. (ii) The absolute magnitude distribution of *Galaxia* shows a mild excess at $M_V \sim 1$ and a slight deficit at $M_V \sim 3$. This excess was also observed by Girardi et al. (2005) and is of comparable magnitude. Again, unlike Girardi et al. (2005) we do not see any deficit in the faint tail ($M_V > 4$). (iii) In the color distribution, the red clump peak at $B - V \sim 1$ is shifted slightly to the red side for *Galaxia* and the blue tail shows a slight excess of stars. As remarked by Girardi et al. (2005) these discrepancies could be due to imperfections in the stellar evolution models or due to imperfect simulation of the parallax errors and should be investigated in future.

Other than the minor differences discussed above, there is one major difference between the two catalogs. The number of stars in the simulated catalog is about 33% higher. This is due to the fact that we have excluded the stellar multiplicity (e.g. unresolved binary systems) from the Hipparcos catalog. For the selection limits used by us the Hipparcos catalog contains about 1549 sources that are flagged as binary. Multiplying this number by two and adding it to the number of single sources (8353) we get a total of about 11451 stars, which is in good agreement with the number of stars in the simulated catalog (11169).

4.3. Comparison with solar neighborhood kinematics from the Geneva-Copenhagen survey

The best kinematic data to date are largely restricted to the solar neighborhood. We now compare these observations with kinematic simulations from *Galaxia*. We use the data from the Geneva-Copenhagen Survey, GCS, (Nordström et al. 2004; Holmberg et al. 2009), which is a selection of 16682 F and G type main sequence stars, out of which velocities and temperatures are available for 13382 stars. The GCS catalog is complete only till $r \sim 40$ pc in volume and $V \sim 8$ in magnitude and within these limits there are only about 1000 stars. Hence,

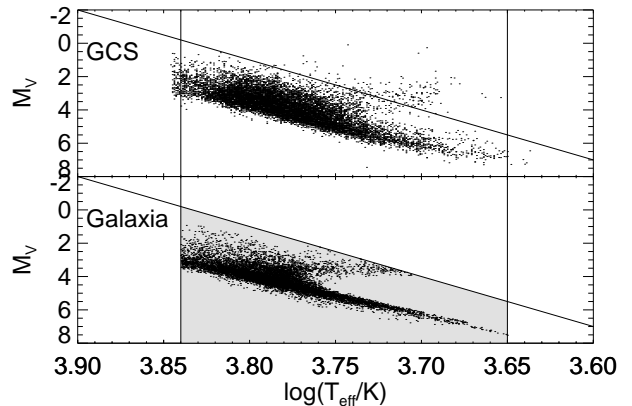


FIG. 6.— Distribution of GCS stars in the (T_{eff}, M_V) plane and the choice of selection functions. The top panel shows the GCS stars lying within $r < 0.12$ kpc and the lower panel shows the stars sampled with *Galaxia*. The shaded region in the lower panel shows the selection region used to mimic the GCS stars. The line represents the equation $M_V = 115 - 30 \log(T_{\text{eff}})$.

to increase our sample size we select stars within 120 pc from the Sun and with $V < 9.6$, 10893 stars were found to satisfy this criteria. A drawback of this is that beyond the completeness limit of the survey, it is not possible to deduce the exact selection functions and these are needed to mimic the GCS catalog with *Galaxia*. However, the incompleteness was found to have little effect on the kinematic properties of the sample. To check this we compared the velocity distributions of the complete and incomplete samples as described above and found them to be nearly identical. Hence, an approximate selection function that can reproduce the main properties of the GCS sample, namely, the selection of F and G type dwarfs with minimal contamination from red giants, should be sufficient for our purpose. To do this, we plot in Figure 6 the distribution of our selected GCS stars, in the (T_{eff}, M_V) plane. The shaded region in the plot shows the desired selection function in the (T_{eff}, M_V) plane, which can be described by the following equations $3.65 < \log(T_{\text{eff}}) < 3.84$ and $M_V < 115.0 - 30 \log(T_{\text{eff}})$. We use this to reproduce the GCS catalog with *Galaxia* and this is shown in the lower panel. The stars generated with *Galaxia* were also restricted to $V < 9.6$ in magnitude and $r < 120$ pc in distance.

Next, in Figure 7, we plot the predicted distributions of the U, V and W component of velocities and compare them to the GCS survey. It can be seen that the model (the red curves) provides a reasonable fit to the distributions of all the three components of velocities. In the plots shown in the panels, the Sun's motion with respect to the local standard of rest (LSR) was assumed to be $U_{\odot} = 11.1$ $V_{\odot} = 12.24$ and $W_{\odot} = 7.25$ as given by Schönrich et al. (2010).

In *Galaxia* we model the distribution of the v_{ϕ} component of velocities using the asymmetric drift relation given by Equation (5). As mentioned earlier, an alternative way to model the v_{ϕ} velocities is to use the Shu distribution function which provides a more accurate treatment of the radial motion in the disc (see Appendix A for further details). In Figure 7 this is shown as the dashed curve. The Shu distribution function (DF) is found to overestimate the negative tail slightly and its peak is also slightly to the right as compared to the one predicted by Equation (5). Using the iterative scheme of Dehnen (1999) one can further improve the accuracy of the solution (dark green solid line in Figure 7), but even this

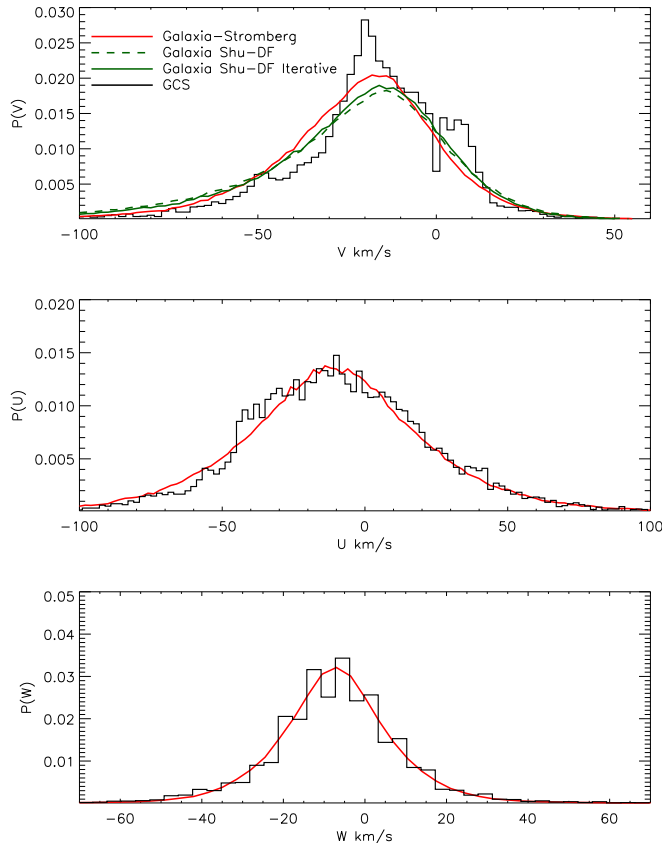


FIG. 7.— Predicted velocity distributions near the Sun. Shown are the U , V and W component of velocities. The dotted lines show the distributions of F and G type stars in the GCS survey of the solar neighborhood (Nordström et al. 2004) ($r < 0.12$ kpc).

has only a marginal effect in resolving the overestimation of the negative tail. On the other hand, lowering σ_{r0} for both the thin and thick disc was found to reduce this discrepancy but this also makes the U distribution sharper than that observed for GCS stars. It should be noted that in the regime $V < -60$ km s $^{-1}$ where the tail is overestimated, Poisson errors are also high, owing to low number of stars, hence we refrain from trying to alter the model to fit the data at this stage. Note, the fact that the Stromberg relation provides a better fit to the negative tail than the Shu DF, is only because it underestimates the negative tail as compared to the distribution expected when radial motions are properly taken into account.

Finally, in a manner similar to Schönrich et al. (2010), our model distributions can also be used to calculate the solar motion with respect to the LSR. To accomplish this we applied a χ^2 minimization scheme and fitted our model U , V , W distributions to the distributions of the GCS stars (a uniform weighting scheme was used). We found $(U_{\odot}, V_{\odot}, W_{\odot}) = (11.25 \pm 0.3, 10.93 \pm 1.2, 7.86 \pm 0.3)$ km s $^{-1}$ (1σ range), which are in good agreement with values of Schönrich et al. (2010). However, our predicted value of V_{\odot} is closer to value reported by Binney (2010) (11 km s $^{-1}$) than that of Schönrich et al. (2010). Note, this result is with the V component of velocity being modeled using the Shu distribution function, if instead the relation given by Equation (5) is used, the best fit value of V_{\odot} is found to be even lower (~ 10 km s $^{-1}$). However, this discrepancy is not significant considering the fact that a

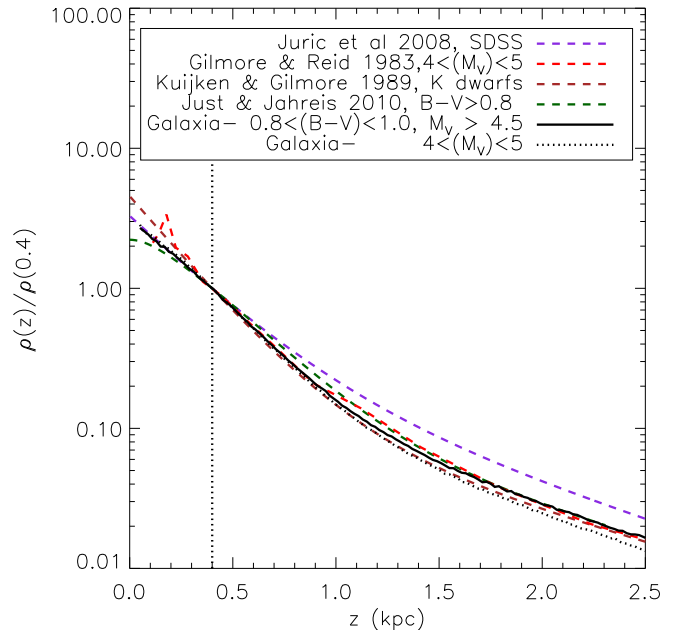


FIG. 8.— Vertical distribution of star counts using *Galaxia* and its comparison with published results.

random uncertainty of about 1 km s $^{-1}$ is associated with it. Moreover, the substructures being quite dominant in the distribution a systematic uncertainty of as high as 2 km s $^{-1}$ is also expected (Schönrich et al. 2010).

4.4. Vertical distribution of stars in the solar neighborhood

Predictions for vertical distribution of stars is another important test for a model. Traditionally the vertical distribution is modeled as a sum of two exponentials representing the thin and the thick disc. The best fit parameters as provided by Jurić et al. (2008) for the M dwarfs in SDSS, after correction for biases, e.g., stellar multiplicity, are a thin disc with a scale length of 300 pc, a thick disc with a scale length of 900 pc, and a local thin to thick disc normalization of $f = 13\%$. Using K dwarfs towards the south galactic pole (SGP), Kuijken & Gilmore (1989) report a value of $f = 4.27\%$ and scale lengths of 249 pc and 1000 pc for the thin and thick discs, respectively. Also using the data towards the SGP, Gilmore & Reid (1983) provide the vertical distribution of stars for different absolute magnitude ranges — we use results reported for magnitude range $4 < M_V < 5$ since stars at higher absolute magnitudes could be contaminated by giants. Figure 8 shows these published results alongside our results using *Galaxia*. Also is shown the results from the model of Just & Jahreiß (2010). Note, we normalize all the profiles to the density at $z = 0.4$ kpc. This is because density estimates close to $z = 0$ cannot be reliably obtained and one has to use interpolation to get the local normalizations, which makes the estimates strongly dependent upon the assumed shape of the profile⁴. Although using the SDSS selection functions would have been ideal for comparing with the predictions of *Galaxia*, the theoretical isochrones

⁴ Interestingly, a compilation from literature of local normalization versus scale height by Arnadottir et al. (2009) seems to suggest that, in spite of a large spread in the values of these quantities, the estimated total mass between different surveys is roughly the same.

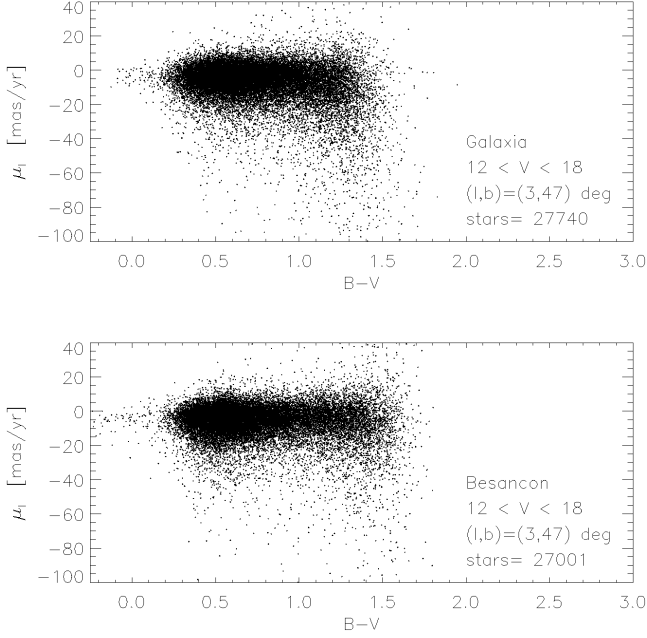


FIG. 9.— Plots of color $B - V$ vs proper motion μ_l towards $(l, b) = (3, 47)^\circ$, for $12 < V < 18$. Upper panel shows results obtained with *Galaxia* while the lower panel shows results from the *Besançon* model.

are not very accurate in the M dwarf regime at the present time. Hence, we use a color range of $0.8 < B - V < 1.0$ and $M_V > 4.5$ to identify the main sequence dwarfs and report the results for them. Our results correspond closest to the plot of Gilmore & Reid (1983). Closer to the plane ($z < 0.5$ kpc) they are also in good agreement with that of Jurić et al. (2008), but at larger distances they differ. We also show the results with stars selected according to their absolute magnitude ($4.0 < M_V < 5.0$). This is quite close to the color limited profile but differs slightly in the regime $z > 1$. This shows the effect of selection bias on the profile. Note, our assumed location of the Sun above the galactic plane (15 pc) is slightly less than that reported by Jurić et al. (2008) (25 pc), but this has negligible impact on the analysis presented here.

4.5. Color vs proper motion comparison

In R03, distributions of color vs proper motion from *Besançon* model were shown and found to be in good agreement with observations of Ojha et al. (1996). Here we repeat the same analysis and compare our results with those of the *Besançon* model (Figure 9). Stars were identified in a 15.5 square degree area in the direction of $(l, b) = (3, 47)^\circ$ and with magnitudes in the range $12 < V < 18$. In upper panel of Figure 9 the bluer region is dominated by the thick disc and the halo, while the redder region is dominated by the thin disc. It can be seen that our distribution is in good agreement with that of the *Besançon* model. However, subtle differences can be identified in the region $1 < B - V < 1.5$. At around $B - V \sim 1.0$, the dispersion of μ_l is slightly less for *Besançon*. Also, the *Besançon* stars extend further redwards. These differences owe their origin to the differences between the isochrones used by us and the *Besançon* model (see Section 4.1).

4.6. Computational performance

We have implemented the scheme in the form of a serial code written in C++. It uses about 500 MB RAM and the amount of memory used is independent of the size of the catalog being simulated. However, the CPU time depends sensitively upon the parameters of the survey being simulated. In what follows, we report CPU times by running the code on a 2.44 GHz single Intel processor.

Recall that in our scheme the Galaxy is divided into roughly equal mass cubical boxes (nodes), and stars are generated from only those nodes that intersect with the survey volume. This causes the run time to vary nearly linearly with the mass of the galaxy being sampled by the survey. Now, for a given survey there are two main parts that consume most of the CPU time: a) time to pre-process a node, and b) time to generate stars in a node. Pre-processing all of the nodes takes about 250 seconds. For surveys sampling a smaller mass fraction, this is also proportionately lower. Generating stars is where the code spends most time and to measure this we define the speed of the code as the number of stars generated per second. The code can reach a maximum speed of 0.2 million stars per second when generating all stars in the galaxy. For magnitude limited surveys, the speed is slightly lower, e.g., a $V < 20$ survey runs at 0.16 million stars per second while a $V < 15$ survey runs at 0.05 million stars per second. The optimization of the code to generate only stars that can enter the catalog is imperfect, especially if a galactic component has a large spread in metallicity. This is something we hope to improve in future.

With the speeds given above, an all-sky GAIA-style survey with $V < 20$, consisting of 4 billion stars can be generated in about 6.5 hours. In comparison, the scheme of Brown et al. (2005) required about 2 weeks to generate a GAIA like sample of 3.5×10^8 stars while running on a cluster of processors. On the other hand, a $V < 20$ survey confined to 10,000 sq degree towards the north galactic pole, consisting of a sample of 3×10^7 stars can be generated in 220 seconds.

Note, running a single instance of the code is sufficient for generating catalogs of sizes up to 10^8 stars in less than half an hour, but for larger catalogs one could easily parallelize the code. Parallelization simply involves running multiple instances of the code, each with a different random seed and generating a fixed fraction of the full galaxy.

5. APPLICATIONS

5.1. All-sky distributions of giants and red clumps

As an application of the code, we investigate the distribution of giants and red clump stars over the sky. We use the following criteria to identify the stars that are giants and red clumps; $T_{\text{eff}} < 5000\text{K}$ and $\log(g) < 3.3$. A subset of these stars having $4500\text{K} < T_{\text{eff}} < 5000\text{K}$ and $1.625 < \log(L/L_\odot) < 1.825$ were identified as red clumps. Figure 10 shows all-sky maps for the fraction of stars that are giants and red clumps, and the ratio of red clump to giants, for a RAVE-style survey with magnitudes in the range $9 < I < 13$. The lower panels show the same but with dust extinction included. Except for the effect of the warp the plots being roughly symmetrical about $l = 180^\circ$, we concentrate on the first half only, i.e., $0^\circ < l < 180^\circ$. It can be seen in Figure 10 that the fraction of stars that are giants and red clumps decreases as a function of l and $|b|$ as one moves away from the galactic center and the galactic mid plane respectively. This is mainly due to the fact that giants being more luminous can be seen farthest in a magnitude limited sample, and for a given solid angle,

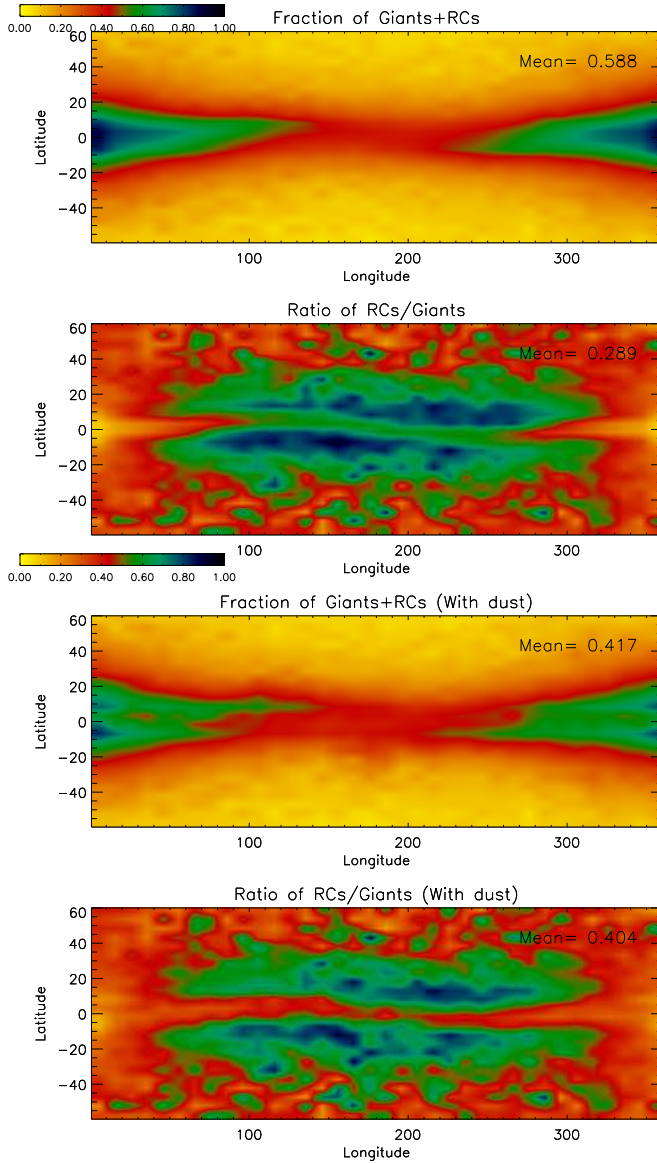


FIG. 10.— Angular distribution of giants and red clumps. Shown are the fraction of giants and red clumps, and the ratio of red clump to giants in a survey with magnitudes in the range $9 < I < 13$. The upper panels are without dust extinction while the lower panels are with dust extinction. In the figures, the small scale structures lying away from the galactic mid plane are due to Poisson noise resulting from low number of stars.

the volume sampled increases as cube of the distance. Hence, in directions where the disc extends the farthest, we should expect to see a higher fraction of giants. Red clumps on the other hand are less luminous than the giants which means that the ratio of red clumps to giants will be lower in regions where the fraction of giants is higher. Additionally, the red clumps are found in metal rich populations only. Now, due to the existence of a vertical metallicity gradient in the disc, as one moves away from the galactic plane the fraction of metal rich population being surveyed decreases, this makes the ratio of RCs/giants to fall off as one moves away from the galactic mid-plane. Including dust extinction in general leads to faint stars getting excluded in a volume limited survey. Since a RAVE-style survey has a significant fraction of giants lying at larger distances, where they also appear faint, the effect of extinction is to lower the overall fraction of giants (from 0.6 to

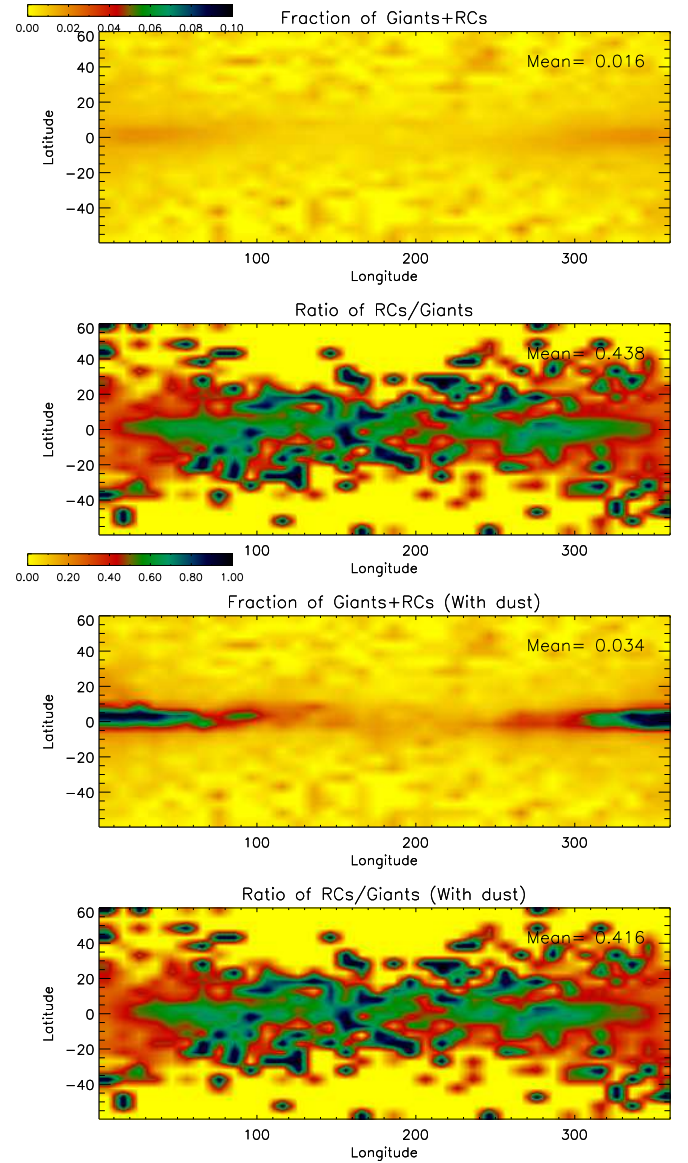


FIG. 11.— Angular distribution of giants and red clumps. Shown are the fraction of giants and red clumps, and the ratio of red clump to giants in a survey with SDSS r band magnitude in the range $4 < r < 22$. The upper panels are without dust extinction while the lower panels are with dust extinction. The color bar range for 1st and 3rd panels is 0 to 0.1 and for 2nd and 4th panels is 0 to 1. In the figures, the small scale structures lying away from the galactic mid plane are due to Poisson noise resulting from low number of stars.

0.4). As expected the overall ratio of red clump stars to giants increases slightly (from 0.3 to 0.4) on including extinction.

Next, we repeat our analysis for an SDSS-style survey, with r band magnitude in the range $4 < r < 22$ (Figure 11). The mean fraction of stars that are giants and red clumps is found to be 0.016, which increases to 0.034 when extinction is included. The mean ratio of red clumps to giants is 0.44, which with extinction included decreases only slightly to 0.42. Here the effect of extinction on the fraction of giants is opposite to what we saw earlier for the RAVE simulation. This is due to the fact that in an SDSS type survey the faint end of the magnitude distribution is dominated by main sequence dwarfs, which get excluded by the effect of extinction. On the other hand, given the extremely faint magnitude limit of the survey, the giants and red clumps in the disc are luminous enough to

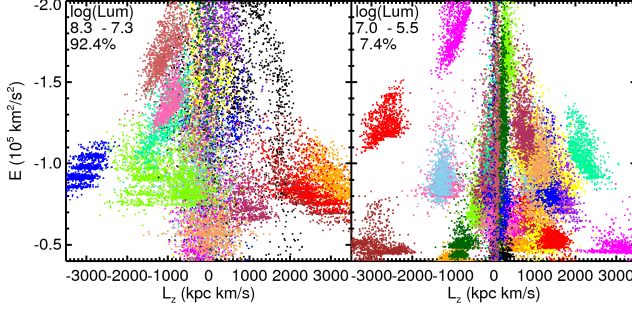


FIG. 12.— Distribution in $E - L_z$ space of particles lying within 150 kpc from the galactic center in one of the BJ05 simulations. 17 unique colors were used with each color representing a different satellite. Left panel shows the 20 most luminous satellite systems while the right panel shows the next 40 most luminous systems. For each panel the range in luminosity in units of $\log(L/L_\odot)$ and its percentage contribution to the total halo is also labelled. Each satellite system is sampled with about 1000 particles and the sampling probability of a particle with in a given satellite is proportional to its luminosity. The satellites were sorted in decreasing order of their luminosity before plotting, so as to make the lower luminosity satellite systems, which are expected to cover a smaller area in the map, lie on top of higher luminosity systems.

be visible even after including the effects of extinction.

5.2. Identification of substructures in the stellar halo in $E - L_z$ space with GAIA

As an application of our code, we assess the ability of the astrometric mission GAIA to identify structures in the stellar halo. Helmi & de Zeeuw (2000) first performed such an analysis and concluded that given the accuracy of GAIA, it would be relatively easy to identify the structures in integrals of motion space, e.g., energy E vs the z component of angular momentum L_z . Subsequently, Brown et al. (2005) showed that in the $E - L_z$ space favored by Helmi & de Zeeuw (2000), the structures are nearly washed out if the background population of stars are taken into account. While Helmi & de Zeeuw (2000) assumed the halo to be formed out of in-falling satellites exclusively, Brown et al. (2005) superimposed a few disrupted satellites onto an otherwise smooth stellar halo. Hence neither of the simulations were done in a proper cosmological context. Recently Gómez et al. (2010) (GHBL hereafter) have done higher resolution simulations similar to Helmi & de Zeeuw (2000) along with some enhancements, in particular, a time dependent analytic potential, and satellite luminosities drawn from the present-day distribution of Milky Way satellites (Koposov et al. 2008). They conclude that significant amount of structure can be seen in the (E, L_z, L) space. We repeat a similar analysis here but using the N-body models of Bullock & Johnston (2005) that simulate the halo in a cosmological context and hence have realistic time-dependence of rate of in-fall and luminosities of accreted satellites.

First we investigate as to how clustered are the particles of a tidally disrupted satellite in $E - L_z$ space and compare them with the results of GHBL. Specifically we reproduce Figure 4 of GHBL showing the distribution in $E - L_z$ space of particles in the simulations with different colors representing different satellites. Results from one of the BJ05 simulations used by us are shown in Figure 12. While GHBL show all 43 satellites simulated by them, we show 20 most luminous satellites in left panel and next 40 luminous in right panel. The 20 most luminous systems which constitute about 92% of the stellar mass are significantly less clustered than the other low lumi-

nosity systems. The Fig-4 in GHBL in fact resembles the right panel, which means that energy and angular momentum is conserved less in BJ05 than in GHBL. Also a lot particles can be seen at low L_z and high E in BJ05 as compared to GHBL suggesting that there are more high energy radial orbits in BJ05 simulations.

Given the differences in the results of GHBL and BJ05, it is imperative to look at the differences between the methodology of the two simulations, so as to isolate the cause.

- Dynamical friction is ignored in GHBL whereas BJ05 use a modified version of the Chandrasekhar dynamical friction formula. Since dynamical friction is strongest for massive systems this will make luminous systems appear fuzzier, an effect seen in BJ05 simulations. This could be one of the reasons for the BJ05 results being fuzzier in general than GHBL.
- In GHBL the stellar particles of a satellite are not explicitly embedded in dark matter potentials. In general one expects embedded satellites to take longer to disrupt and moreover they disrupt in parts with each pericentric passage redistributing the energy and hence leading to more non conservation of energy.
- In BJ05 the satellites are evolved from the time since they were accreted to the host halo whereas in GHBL all satellites are evolved for 10 Gyrs. As a consequence in BJ05 one expects older systems to be fuzzier and young systems to be clustered.
- In GHBL the orbit initial conditions are drawn from a distribution function corresponding to the density profile of the stellar halo at $z=0$ whereas in BJ05 they are motivated from cosmological simulations. The overall effect of this on the results is not clear.

Next, we investigate the prospect of detecting the structures in the stellar halo with GAIA. The parallax and photometric errors of GAIA increase steeply beyond $V \sim 15$, hence GAIA will be most accurate for nearby and/or bright stars. Hence similar to GHBL we generate a solar neighborhood sample of stellar halo stars, using BJ05 simulations, with the following constraints— $V < 16$, $M_V < 4.5$ and $r < 4$ kpc. This resulted in a sample of 1.3×10^5 stars, which is similar but slightly larger than that of GHBL (0.8×10^5). In Figure 13 we show a density map of stars in the $E - L_z$ space. In the left panel the stars have same phase space coordinate as that of their parent N-body particle, whereas in the right panel the spawned stars are distributed in phase space according to the scheme mentioned in Section 2.4. It can be seen that dispersing the spawned stars in phase space has a disastrous effect of smoothing out the distribution of stars. In the top panels, we show the distribution of stars a single satellite system. It can be seen that even in the original N-body coordinates (top left panel) the stars are not strongly clustered. Spawning stars from it makes the situation even more worse (top right panel). The problem stems from the limited numerical resolution of BJ05 simulations, specially a few massive ones which dominate most of the mass in the stellar halo. Within 4 kpc from the Sun, typically a satellite contributes about 200 particles, and the range of scales covered in velocity space is of the order of $\pm 200 \text{ km s}^{-1}$. Now, considering the fact that we smooth over 64 particles in phase space, it is easy to see that large amount of scatter is introduced when spawning multiple stars from a

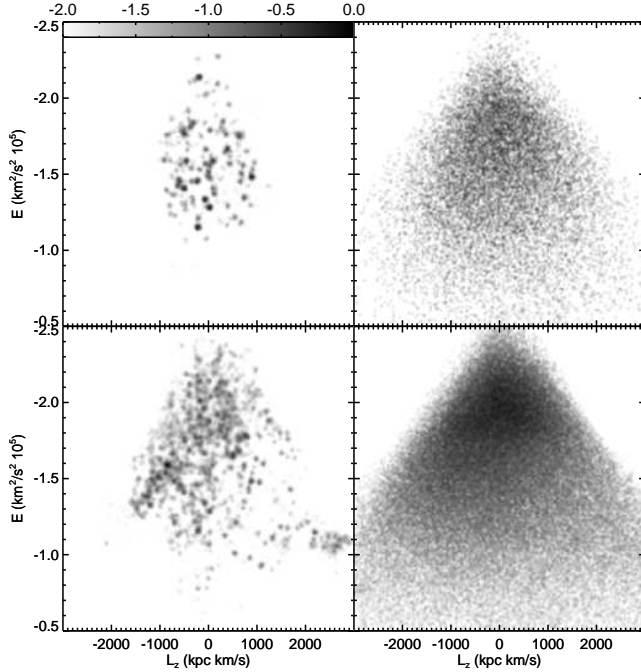


FIG. 13.— Number density map in $E - L_z$ space of stars lying within 4 kpc from the sun in one of the BJ05 simulations. Top panels: stars from a single satellite. Bottom panels: all stars. In the left panels, stars have the same phase space coordinate as that of their parent N-body particles. This means multiple stars can have same phase space coordinates. Hence, for the aid of visibility, a dispersion of 30 kpc km s^{-1} along L_z and $1000 \text{ km}^2 \text{ s}^{-2}$ along E was added to the position of stars in the left panels. The color table represents $\log(\rho_{\text{max}}/\rho)$, ρ being the number density.

single particle. Additionally, L_z being a product of position and velocity coordinates, even a small amount of dispersion in position and velocity coordinates can cause a large spread in the value of L_z . Incidentally, GHBL were able to identify significant substructure in their analysis. However, due to the above mentioned limitations we cannot do a faithful comparison with the results of GHBL.

5.3. Substructures in the stellar halo in (x, y, z) and (r, v_r) space

According to our discussion in Section 5.2 it is clear that when multiple stars are spawned from a single N-body particle significant smoothing of structures occurs. Hence, it is imperative to check the regime in which the results are reliable.

In Sharma et al. (2010a,b), an application of the code was shown for identification of structures in 3d (x, y, z) space making use of the photometric information of stars. Note, when kinematics are not needed the sampling resolution can be improved by calculating the smoothing lengths in 3d position space only. Moreover, a smaller number of smoothing neighbors, typically 32, can be used. This improves the spatial resolution by a factor of 3 on average when compared to smoothing lengths in 6d space with 64 neighbors. To check this in Figure 14 we plot the surface density maps of stars of a simulated halo as sampled by *Galaxia*. A color limit of $0.1 < g - r < 0.3$ (SDSS g and r band) and magnitude limit of $r < 27.5$ was used to sample the main sequence stars, so as to fairly sample all the relevant stellar populations in the halo. A sub-sampling factor of $f_{\text{sub-sample}} = 0.25$ was used which resulted in about 1.5×10^7 stars. A slice with $|y| < 10 \text{ kpc}$ was selected to make the plots. The top left panel shows the map

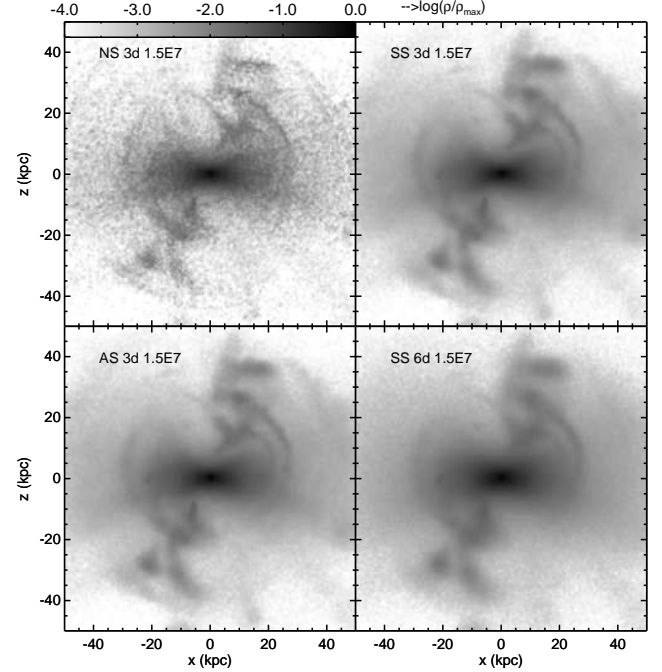


FIG. 14.— Number density map of stars in $x - z$ space of a simulated halo sampled by *Galaxia* at a resolution of 1.5×10^7 with different sampling schemes (NS, AS, SS). The bottom right panel is sampled in 6d while the rest of the panels are sampled in 3d.

as produced when the stars have the same phase space coordinates as that of the original N-body particle (no scatter scheme NS). The top right panel shows the results with the default sampling scheme of *Galaxia* where the stars are scattered only when an N-body particle spawns more than one stars (selective scatter scheme SS). The bottom left panel show the maps when all the spawned stars are scattered (all scatter scheme AS). The bottom right panel shows the map when the stars are sampled in 6d phase space. At such a high sampling resolution nearly all N-body particles spawn more than one star, hence the SS-3d and AS-3d results are identical. Comparing SS-3d with NS panel it can be seen that all the visible structures in NS are adequately reproduced by *Galaxia*. However, extremely low contrast structures in the outskirts in the form of shells are smoothed out. The SS-6d scheme also reproduces the prominent structures correctly, but in general its results are slightly more smoothed when compared to SS-3d, which is expected as working in higher dimensions erodes the spatial resolution.

Next, we look at the prospect of analyzing the data when radial velocity information is also available. Recently two point correlation function in (x, y, z, v_r) 4d space has been used to quantify the amount of structure in the stellar halo (Xue et al. 2010; Cooper et al. 2010a; Starkenburg et al. 2009). Typically when comparing theory with observations the age and metallicity distribution of all the N-body particles is assumed to be same. In BJ05 simulations each progenitor has its own stellar population and with *Galaxia* it is now possible to draw stars using this information. In Sharma et al. (2010a) it was shown that depending upon the color and magnitude cuts employed the sampling probability is different for different accretion events.

In Figure 15 we show the number density map of stars in the $r - V_r$ space (radial distance and radial velocity with respect to galactic center). The top, middle and bottom panels show

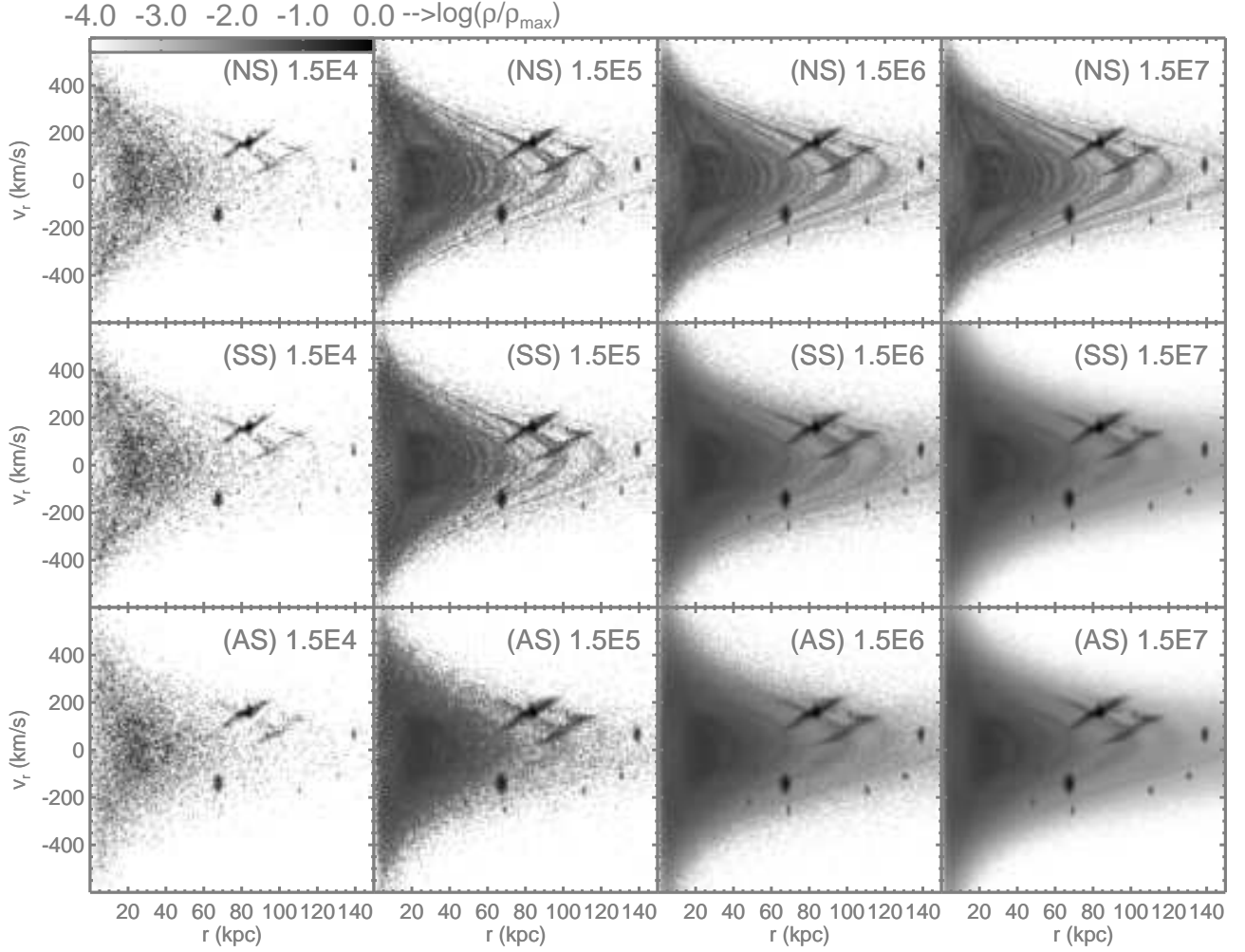


FIG. 15.— Number density map of stars in $r - V_r$ space (radial distance and radial velocity with respect to galactic center) of a simulated halo sampled by *Galaxia* at different resolutions (1.5×10^4 to 1.5×10^7) and different scattering schemes (NS, AS, SS). Label NS stands for no scattering scheme, where the stars are simply assigned the co-ordinates of its parent N-body particle. Label SS stands for the improved selective scattering scheme, where the stars are scattered only if its parent N-body particle generates more than one star. Finally, label AS stands for the scheme where all the spawned stars are scattered.

the results with NS, SS and AS scheme respectively. The sampling resolution increases from left to right in the plots. A sub-sampling factor of $f_{\text{sub-sample}} = 0.25, 0.025, 0.0025$ and 0.00025 were used which resulted in sample sizes of 1.5×10^4 , 1.5×10^5 , 1.5×10^6 and 1.5×10^7 respectively. The fraction of stars, that suffer from scattering in the default SS scheme, is 3, 25, 70 and 93% for sample sizes ranging from 1.5×10^4 to 1.5×10^7 (bound systems, which are anyway easily detectable, were excluded). Hence, for sample sizes below 10^5 very few stars need to be scattered. This fact is also reflected in the maps in Figure 15, where, at resolutions below 1.5×10^5 the maps of NS and SS scheme are almost identical. In contrast, the AS scheme significantly erodes the structures. At resolution of 10^6 , the SS scheme is better than AS but when compared to the NS scheme, structures below $r < 50$ kpc are eroded. At even higher resolution, the SS scheme is identical to AS scheme, which is expected as 93% of the stars are scattered. At the highest resolution, most prominent structures are correctly reproduced but the contrast of the fine scale structures is reduced. Note, these results are without observational errors, which when included will anyway erode the fine scale, low contrast structures. To summarize, we think the results from *Galaxia* when sampling the stellar halo in 6d space

have excellent reliability for resolutions $N < 10^5$, and for $N = 10^6$, moderate reliability only beyond 50 kpc. In other regimes slight smoothing can be expected but the results will still be reliable wherever the observational errors are larger than the smoothing effects induced by our star spawning process.

We now discuss the nature of our scattering errors. The uncertainties that arise from our N-body sampling scheme are very different from normal observational errors. To begin with, our sampling scheme is more like an interpolation of a function. This means that if the function (density field) is smooth the errors are small. Next, if the number of points over which the function is known is large (numerical resolution of the simulations), the errors will again be small. Finally, the amount of scattering in our scheme is inversely proportional to the number density of particles, this means that the scattering effects are inherently adaptive in space and this is one of the strengths of our scheme. For example, the detectability of a structure depends upon its density peak being correctly resolved in space and this being a high density region has lower amount of scattering associated with it. Incidentally, the adaptive nature of scattering can also be a weakness in some cases. For example, if a low particle density region of another sys-

tem contributes significantly to the number density of stars at the location of a given structure then it can decrease the contrast of that structure. This is typically the case in our simulations, where the smooth background component of the halo is dominated by a few massive accretion events which are not adequately resolved. Hence the weakness is not really a drawback of the scheme but more an artifact of inadequate particle resolution of simulations. The question as to what is the appropriate N-body resolution for simulating a structure so that it can be properly sampled by our scheme, is something which should be tested in future by numerical convergence studies of simulations with different resolutions.

Finally, we discuss as to which type of accreting systems are most likely to suffer from scattering. The BJ05 simulations sample all satellites with typically same number of stellar particles (approximately 2×10^4) irrespective of their luminosity, this means low luminosity systems are less likely to spawn multiple stars and suffer from scattering as compared to the high luminosity ones. Moreover, the low luminosity systems are less phase mixed and have high particle phase space density (as they have smaller internal velocity dispersions and are less affected by dynamical friction), and hence these systems will also have lower amount of scattering. Finally, dynamical friction sinks the systems inwards and it being stronger for the high luminosity systems, such systems will lie preferentially towards the inner regions of the halo than the outskirts. This explains the smoothing in the plots being more prominent in the inner regions ($r < 50$ kpc).

6. DISCUSSION

Presently, given a model the code generates a particular realization of it. While this has its own applications, e.g., testing instrument capabilities, correcting for systematics and making predictions for observations. But in the end one desires to learn more about the formation of our galaxy. And this would require refining or fine tuning the model as new data comes in. In this respect, our parameterized analytical models based on well understood physical principles easily lend themselves to model fitting procedures and are an invaluable tool for understanding the formation of our galaxy. Such schemes have been successfully used to constrain the star formation rate and the age-velocity relation by using the data in the solar neighborhood (Aumer & Binney 2009; Just & Jahreiß 2010). A fast and efficient method to generate surveys from parameterized models as presented here should be immensely useful for performing such model fitting analysis in future. More generally one could use the Markov Chain Monte Carlo schemes (Lewis & Bridle 2002) to explore the parameter space of the analytical models.

In order to facilitate the exploration of the parameter space there are two issues that need to be addressed. First, although one can vary the SFR and other model parameters that exist in *Galaxia*, dynamical consistency is not guaranteed. This can be done by using the scheme outlined in Bienayme et al. (1987) (see also Just & Jahreiß (2010)), where they self-consistently calculate the local scale height (or alternatively the ellipticity) as a function of age. Note, in the above scheme the large scale dynamical self consistency is still not guaranteed. Secondly, although *Galaxia* is fast enough to generate multiple realizations of a model but each time the model is changed the code needs to recompute the nodes which takes some time. This is also something that can be improved.

Chemical evolution is also another thing that is presently not self consistent. Recently some promising semi-analytic

schemes have been proposed in which chemical evolution is done along with radial mixing (Schönrich & Binney 2009). Although presently in *Galaxia* we do not include models with radial mixing but we have shown that in principle it is possible to accommodate this within our framework.

There are also some other improvements that can be done. *Galaxia* has yet to incorporate a detailed central bar (presently only a bar shaped bulge is included) and the spiral arms because these await better constraints from the AAOmega survey of the central disc (K.C. Freeman, personal communication). Although presently in *Galaxia*, the thick disc is treated as a population of constant age in the manner of the Besançon model. This is in agreement with Freeman & Bland-Hawthorn (2002), who consider the thick disc to be chemically distinct (Bensby et al. 2003, 2005) and uniformly old (Gilmore et al. 1995). However, there are alternative models, e.g., Schönrich & Binney (2009) model the thick disc by scattering stars from the inner regions of the disc. Here the thick disc is also old but not necessarily of a constant age.

Finally, as an application we plan to use *Galaxia* to address one of the key goals of the HERMES project, i.e., recovering star clusters that have long since dispersed within the Galaxy. The ability to recover ancient star clusters for a given set of observational parameters can be tested using a multi-dimensional group finding algorithm Sharma & Johnston (2009). The power of this approach was recently demonstrated in the context of simulated dwarf galaxies (Bland-Hawthorn et al. 2010a). With *Galaxia* for a given observational survey one can estimate the mass in different galactic components. Subsequently, simple prescriptions assuming an initial cluster mass function for stars along with the assumption of chemical homogeneity within a cluster could be employed to simulate structures in the chemical abundance space.

7. CONCLUSIONS

It is only in recent times that the community has begun to undertake massive spectroscopic surveys of 10^5 to 10^6 stars. These include the RAVE survey on the UK Schmidt 1.3m telescope (Steinmetz et al. 2006), the APOGEE (Majewski et al. 2010) and SEGUE surveys (Yanny et al. 2009) on the Sloan 2.3m telescope and the upcoming HERMES survey on the AAT 3.9m telescope (Freeman & Bland-Hawthorn 2008). Similar surveys are under discussion for the LAMOST and the CFHT (3.6m) telescopes. These surveys are to be complemented by huge astrometric missions, in particular, JASMINE (Yano et al. 2008) and GAIA (Perryman 2002), and all-sky photometric surveys from SkyMapper (Keller et al. 2007), PanSTARRS and LSST (Ivezic et al. 2009). Thus, within a decade, we will have a vast wealth of data over a significant fraction of the Galaxy.

If we are to move beyond information to knowledge, a working framework will be essential. This framework needs to be sufficiently flexible that it can adapt to new developments in the theory of galaxy dynamics, updates in stellar synthesis libraries, and ever-improving N-body or semi-analytic simulations. On the other hand, the framework should also be fast enough to generate huge amounts of data and multiple realizations in preparation for upcoming surveys. To this end, we have presented here a population synthesis code for generating a synthetic catalog of stars from a given analytical or N body model of a galaxy. A set of theoretical isochrones are used to convert the given model into a catalog of stars.

Although schemes for converting an analytical model into stellar catalogs have been implemented in the past, but they give catalogs along specific lines of sight rather than a field of finite size and its too cumbersome to build a wide field by decomposing it into many line of sights. This makes them limited in their use for generating large wide area catalogs. To overcome this limitation, we implement a new algorithm for sampling the stars that on one hand generates stars that are smoothly distribution over the desired space and on the other hand, is very efficient at generating wide area surveys consisting of a large number of stars. As a concrete example we have implemented the Besançon model within *Galaxia* and shown that it can accurately reproduce Besançon star counts. However, the design of *Galaxia* is flexible enough to simulate other alternative models also. *Galaxia* in general can accept an input model in the form of analytic functions for the density distribution, SFR, AMR and AVR.

In addition to sampling an analytical model, an algorithm for sampling an N body model is also presented. The novel feature of this algorithm is its ability to sample the stars in accordance with the underlying phase space density of the N-body particles. As an application we make use of the simulated N-body models of the stellar halo by Bullock & Johnston (2005) which allows one to make detailed predictions about the structures in the stellar halo. Other than this, the N-body sampling scheme will also be useful to simulate known structures in the Milky Way, e.g., the streams of the Sagittarius dwarf galaxy. Although the N-body sampling scheme is quite robust but if the N-body resolution of the simulations is not adequate then this can lead to spurious smoothing of the structures being sampled.

Using the N-body sampling scheme, we simulated a hypothetical GAIA catalog of stars within 4 kpc of the sun and analyzed the prospect of identifying structures in the energy and angular momentum space, as in Gómez et al. (2010). We

find that due to limited numerical resolution of the simulated stellar halos, our sampling scheme leads to significant wash out of structures. However, even if the sampling scheme is not used, the distribution of the N-body particles of satellites in BJ05 simulations is less clustered as compared to results reported by Gómez et al. (2010). This is something that should be investigated in future.

Although, it is difficult to make very accurate predictions in the solar neighborhood, but we show that the BJ05 simulations are suitable for analyzing deep large scale surveys of the stellar halo. Our analysis shows that the results from *Galaxia* when sampling the stellar halo in 6d space are very reliable for sample sizes of $N < 10^5$, e.g., a survey of RR Lyrae or BHB stars. In other regimes, slight smoothing can be expected but the results will still be reliable whenever the observational errors are larger than the smoothing effects induced by our star spawning process. Additionally, when working in 3d position space the smoothing effects can be reduced by calculating the smoothing lengths in 3d position space only. Our results show that in 3d position space most of the structures are accurately reproduced irrespective of sample sizes.

In conclusion, we have presented a detailed framework that will allow present and future stellar surveys to be compared and evaluated consistently. To facilitate its wider use, we plan to release the *Galaxia* code publicly at <http://galaxia.sourceforge.net>.

ACKNOWLEDGMENTS

JBH is funded through a Federation Fellowship from the Australian Research Council (ARC). SS is funded through ARC DP grant 0988751 which supports the HERMES project. JBH also acknowledges the kind hospitality of Merton College, Oxford, and a visiting professorship from the Leverhulme Foundation during the Hilary and Trinity terms 2010.

APPENDIX

ROTATIONAL KINEMATICS OF THE DISC

The simplest scheme to describe the azimuthal velocity distribution is to consider it in the form of a Gaussian along with a term to correct for the asymmetric drift (see equation 4). A more thorough treatment is obtained by assuming the Shu (1969) distribution function

$$f_{\text{Shu}}(E, L) = \frac{\gamma(L)\Sigma(L)}{2\pi\sigma_R^2(L)} \exp\left(\frac{E_c(L) - E}{\sigma_R^2(L)}\right) \quad (\text{A1})$$

where E_c is the energy of a circular orbit with angular momentum L and

$$\gamma^2(L) = 2 / \left(1 + \frac{d \ln v_c}{d \ln R_L}\right), \quad (\text{A2})$$

$R_L = R_c(L)$ being the radius of the circular orbit.

The rms radial dispersion and the surface density is then given by

$$\sigma_R'^2(R) = \frac{\sqrt{2\pi}}{R\Sigma(R)} \int \frac{\gamma(L)\Sigma(L)}{2\pi} \sigma_R(L) \times \exp\left(\frac{\Phi_c(L) - \Phi_{\text{eff}}(R, L)}{\sigma_R^2(L)}\right) dL \quad (\text{A3})$$

$$\Sigma'(R) = \frac{\sqrt{2\pi}}{R} \int \frac{\gamma(L)\Sigma(L)}{2\pi\sigma_R(L)} \times \exp\left(\frac{\Phi_c(L) - \Phi_{\text{eff}}(R, L)}{\sigma_R^2(L)}\right) dL. \quad (\text{A4})$$

(Schönrich & Binney 2009). Starting with values of $\sigma_R(L) = \sigma'_R(L)$ and $\Sigma(L) = \Sigma'(L)$, (primed quantities being target distributions supplied a priori) one can solve iteratively for the values of $\Sigma(L)$ and $\sigma_R(L)$ using the formalism of Dehnen (1999). The distribution of L and hence $v_\phi = L/R$, at a given point R is then given by

$$P(L, R) = \frac{\gamma(R_L)\Sigma(R_L)}{2\pi\sigma_R(R_L)} \exp\left(\frac{\Phi_c(L) - \Phi_{\text{eff}}(R, L)}{\sigma_R^2(R_L)}\right) \quad (\text{A5})$$

where $\Phi_c(L) = \Phi(R_L) + L^2/2R_L^2$ and $\Phi_{\text{eff}}(R, L) = \Phi(R) + L^2/2R^2$ (Schönrich & Binney 2009). For a given rotation curve the potential is computed as $\Phi(R) = -\int_R^\infty v_c^2(R')dR'/R'$. For simplicity we assume a flat rotation curve with $v_c = 226.84$.

Note, σ_R is also a function of age. Hence, in practise, we calculate the functions $\sigma_R(L)$ and $\Sigma(L)$ for a finite set of ages, and then use the simple nearest neighbor interpolation to calculate the $P(L, R)$ for any given age.

REFERENCES

- Arce, H. G., & Goodman, A. A. 1999, *ApJ*, 512, L135
 Arnadottir, A. S., Feltzing, S., & Lundström, I. 2009, 254, 5P
 Ascasibar, Y., & Binney, J. 2005, *MNRAS*, 356, 872
 Athanassoula, E., & Misiriotis, A. 2002, *MNRAS*, 330, 35
 Aumer, M., & Binney, J. J. 2009, *MNRAS*, 397, 1286
 Bahcall, J. N., & Soneira, R. M. 1980a, *ApJ*, 238, L17
 —. 1980b, *ApJS*, 44, 73
 —. 1984, *ApJS*, 55, 67
 Bensby, T., Feltzing, S., & Lundström, I. 2003, *A&A*, 410, 527
 Bensby, T., Feltzing, S., Lundström, I., & Ilyin, I. 2005, *A&A*, 433, 185
 Bertelli, G., Bressan, A., Chiosi, C., Fagotto, F., & Nasi, E. 1994, *A&AS*, 106, 275
 Bienayme, O., Robin, A. C., & Creze, M. 1987, *A&A*, 180, 94
 Binney, J. 2010, *MNRAS*, 401, 2318
 Binney, J., & Merrifield, M. 1998
 Binney, J., & Tremaine, S. 2008
 Bland-Hawthorn, J., Karlsson, T., Sharma, S., Krumholz, M., & Silk, J. 2010a, *ApJ*, 721, 582
 Bland-Hawthorn, J., Krumholz, M. R., & Freeman, K. 2010b, *ApJ*, 713, 166
 Blitz, L. 1993, 278, 98
 Bond, N. A., et al. 2010, *ApJ*, 716, 1
 Brown, A. G. A., Velázquez, H. M., & Aguilar, L. A. 2005, *MNRAS*, 359, 1287
 Bullock, J. S., & Johnston, K. V. 2005, *ApJ*, 635, 931
 Cambrésy, L., Jarrett, T. H., & Beichman, C. A. 2005, *A&A*, 435, 131
 Chabrier, G., Baraffe, I., Allard, F., & Hauschildt, P. 2000, *ApJ*, 542, 464
 Chou, M., Cunha, K., Majewski, S. R., Smith, V. V., Patterson, R. J., Martínez-Delgado, D., & Geisler, D. 2010, *ApJ*, 708, 1290
 Colless, M., et al. 2001, *MNRAS*, 328, 1039
 Cooper, A. P., Cole, S., Frenk, C. S., & Helmi, A. 2010a, *ArXiv e-prints*
 Cooper, A. P., et al. 2010b, *MNRAS*, 406, 744
 De Lucia, G., & Helmi, A. 2008, *MNRAS*, 391, 14
 Dehnen, W. 1999, *AJ*, 118, 1201
 Drimmel, R., Cabrera-Lavers, A., & López-Corredoira, M. 2003, *A&A*, 409, 205
 Dwek, E., et al. 1995, *ApJ*, 445, 716
 Eisenhauer, F., Schödel, R., Genzel, R., Ott, T., Tecza, M., Abuter, R., Eckart, A., & Alexander, T. 2003, *ApJ*, 597, L121
 ESA. 1997, *VizieR Online Data Catalog*, 1239, 0
 Font, A. S., Johnston, K. V., Bullock, J. S., & Robertson, B. E. 2006, *ApJ*, 638, 585
 Freeman, K., & Bland-Hawthorn, J. 2002, *ARA&A*, 40, 487
 —. 2008, 399, 439
 Fux, R. 1999, *A&A*, 345, 787
 Gilmore, G., & Reid, N. 1983, *MNRAS*, 202, 1025
 Gilmore, G., Wyse, R. F. G., & Jones, J. B. 1995, *AJ*, 109, 1095
 Girardi, L., Bertelli, G., Bressan, A., Chiosi, C., Groenewegen, M. A. T., Marigo, P., Salasnich, B., & Weiss, A. 2002, *A&A*, 391, 195
 Girardi, L., Bressan, A., Bertelli, G., & Chiosi, C. 2000, *A&AS*, 141, 371
 Girardi, L., Grebel, E. K., Odenkirchen, M., & Chiosi, C. 2004, *A&A*, 422, 205
 Girardi, L., Groenewegen, M. A. T., Hatziminaoglou, E., & da Costa, L. 2005, *A&A*, 436, 895
 Gomez, A. E., Grenier, S., Udry, S., Haywood, M., Meillon, L., Sabas, V., Sellier, A., & Morin, D. 1997, 402, 621
 Gómez, F. A., Helmi, A., Brown, A. G. A., & Li, Y. 2010, *MNRAS*, 1196
 Haywood, M., Robin, A. C., & Creze, M. 1997a, *A&A*, 320, 428
 —. 1997b, *A&A*, 320, 440
 Helmi, A., & de Zeeuw, P. T. 2000, *MNRAS*, 319, 657
 Holmberg, J., Nordström, B., & Andersen, J. 2009, *A&A*, 501, 941
 Howard, C. D., Rich, R. M., Reitzel, D. B., Koch, A., De Propriis, R., & Zhao, H. 2008, *ApJ*, 688, 1060
 Howard, C. D., et al. 2009, *ApJ*, 702, L153
 Ibata, R. A., Gilmore, G., & Irwin, M. J. 1995, *MNRAS*, 277, 781
 Ivezić, Z., et al. 2009, in *Bulletin of the American Astronomical Society*, Vol. 41, Bulletin of the American Astronomical Society, 366+
 Izumiura, H., Deguchi, S., Hashimoto, O., Nakada, Y., Onaka, T., Ono, T., Ukita, N., & Yamamura, I. 1995, *ApJ*, 453, 837
 Johnston, K. V., Bullock, J. S., Sharma, S., Font, A., Robertson, B. E., & Leitner, S. N. 2008, *ApJ*, 689, 936
 Jurić, M., et al. 2008, *ApJ*, 673, 864
 Just, A., & Jahreiß, H. 2010, *MNRAS*, 402, 461
 Keller, S. C., et al. 2007, *Publications of the Astronomical Society of Australia*, 24, 1
 Kozlov, S., et al. 2008, *ApJ*, 686, 279
 Kuijken, K., & Gilmore, G. 1989, *MNRAS*, 239, 605
 Lewis, A., & Bridle, S. 2002, *Phys. Rev. D*, 66, 103511
 Majewski, S. R., Wilson, J. C., Hearty, F., Schiavon, R. R., & Skrutskie, M. F. 2010, 265, 480
 Marigo, P., & Girardi, L. 2007, *A&A*, 469, 239
 Marigo, P., Girardi, L., Bressan, A., Groenewegen, M. A. T., Silva, L., & Granato, G. L. 2008, *A&A*, 482, 883
 Marshall, D. J., Robin, A. C., Reylé, C., Schultheis, M., & Picaud, S. 2006, *A&A*, 453, 635
 Menzies, J. W. 1990, 35, 115
 Nordström, B., et al. 2004, *A&A*, 418, 989
 Ojha, D. K., Bienayme, O., Robin, A. C., Creze, M., & Mohan, V. 1996, *A&A*, 311, 456
 Perryman, M. A. C. 2002, *Ap&SS*, 280, 1
 Rattenbury, N. J., Mao, S., Debattista, V. P., Sumi, T., Gerhard, O., & de Lorenzi, F. 2007, *MNRAS*, 378, 1165
 Reid, M. J. 1993, *ARA&A*, 31, 345
 Robertson, B., Bullock, J. S., Font, A. S., Johnston, K. V., & Hernquist, L. 2005, *ApJ*, 632, 872
 Robin, A., & Creze, M. 1986, *A&A*, 157, 71
 Robin, A. C., Reylé, C., Derrière, S., & Picaud, S. 2003, *A&A*, 409, 523
 Schlegel, D. J., Finkbeiner, D. P., & Davis, M. 1998, *ApJ*, 500, 525
 Schönrich, R., & Binney, J. 2009, *MNRAS*, 396, 203
 Schönrich, R., Binney, J., & Dehnen, W. 2010, *MNRAS*, 403, 1829
 Sharma, S., & Johnston, K. V. 2009, *ApJ*, 703, 1061
 Sharma, S., Johnston, K. V., Majewski, S. R., Bullock, J., & Muñoz, R. R. 2010a, *ArXiv e-prints*
 Sharma, S., Johnston, K. V., Majewski, S. R., Muñoz, R. R., Carlberg, J. K., & Bullock, J. 2010b, *ApJ*, 722, 750
 Sharma, S., & Steinmetz, M. 2006, *MNRAS*, 373, 1293
 Shu, F. H. 1969, *ApJ*, 158, 505
 Spaenhauer, A., Jones, B. F., & Whitford, A. E. 1992, *AJ*, 103, 297
 Starkenburg, E., et al. 2009, *ApJ*, 698, 567
 Steinmetz, M., et al. 2006, *AJ*, 132, 1645
 Terndrup, D. M., Sadler, E. M., & Rich, R. M. 1995, *AJ*, 110, 1774
 Turon, C., et al. 1992, *ESA Special Publication*, 1136
 van Leeuwen, F. 2007, *A&A*, 474, 653
 Vieira, K., et al. 2007, *AJ*, 134, 1432
 Xue, X., et al. 2010, *ArXiv e-prints*
 Yanny, B., et al. 2009, *AJ*, 137, 4377
 Yano, T., Gouda, N., Kobayashi, Y., Yamada, Y., Tsujimoto, T., Suganuma, M., Niwa, Y., & Yamauchi, M. 2008, 248, 296
 Zhao, H. 1996, *MNRAS*, 283, 149
 Zhao, H., Rich, R. M., & Biello, J. 1996, *ApJ*, 470, 506